A MICROMACHINED DC ELECTRIC FIELD SENSOR USING A TORSIONAL MICRO MIRROR

By:
Janaranjana Sampath Hiniduma
Liyanage

A Thesis submitted to the Faculty of Graduate Studies of The University of Manitoba in partial fulfilment of the requirements of the degree of

MASTER OF SCIENCE

Department of Electrical and Computer Engineering
University of Manitoba
Winnipeg

Abstract

This thesis presents a MEMS dc electric field sensor with wide measurement range and adjustable sensitivity. The novel concept is applying two opposite bias voltage on the sensor surface causing to tilt, enabling operation without reference ground. The sensor mirror is mounted by torsional springs and fabricated using buck micro machining technology. With compared to earlier works with vertical moving MEMS sensors, higher sensitivity is achieved for the same bias voltage. The sensor has an adjustable linear measurement range from 10's V/m to MV/m, with no saturation. Employing on-board electronics to enable independent resonant operation, a resolution of 3.2 V/m was achieved.

A portable semi automated measurement system was developed for outdoor electric field measurements. This overcomes the limit of electric field measurements for lab environments only. With the developed system, dc electric field tests were performed at University Manitoba High Voltage Laboratory, with and without corona presence to simulate an actual power line conditions. Promising results were obtained for future power industry related applications.

Acknowledgements

First and foremost, I would like to express my sincere gratitude to my advisor Dr. Cyrus Shafai for the continuous support for my Master's Degree. It has been an honor and a privilege to work under you. Your patience, motivation, and discussions inspired me to do better everyday. I could not have imagined having a better advisor and mentor for my graduate studies.

I'm very much thankful to Dr. Athula Rajapakse for his invaluable knowledge shared during research discussions and as well as during course work.

A special thank goes to all my colleagues Byoungyoul Park, Tao Chen, Yu Zhou, and Elnaz Afsharipour for their support in my research.

I would like to thank Manitoba Hydro for financially supporting this research and also for the valuable feedback received.

I thank graduate advisor Amy Dario for her support. I would also like to thank Nanofabrication Laboratory manager Dwayne Chrusch for clean room taining and initial enclosure box design, ECE department technical staff for their support for enclosure box design, mechanical engineering technologist Dave Tataryn for machining acrylic design for the sensor mount, and undergraduate student Kristjan Jacobson for initial enclosure box design.

I would like to thank all my friends in Winnipeg for their support during these three years.

At last but not the least, I would like to thank my parents, sister Aunpama and my wife Harshani, who stood by me through good times and bad.

Contents

List of Tables

List of Figures

To my wife....

Chapter 1

Introduction

This thesis presents the modeling, designing and fabrication of a Micro Electro Mechanical Systems (MEMS) based dc electric field sensor and development of an on board electronic measuring system to measure electric field in indoor and outdoor environments.

1.1 Electric Field Measurement

Electric field measurement has been used in a vast range of measuring applications and studied for more than an half a century. For instance, electric field measurements can be used to determine low voltage generated from metal corrosion to ultra high voltage generated form high voltage dc power lines [8]. In power industry, electric field measurements are used to test insulators and to remotely monitor the voltage of transmission lines. In HVdc power transmission, electric charge density near the power lines considered as a critical factor. The electric field level under

the power line determines the maximum allowable time for a human being safely be in that environment without any hazards.

Manitoba Hydro is a power utility company in Manitoba, Canada and is the only power provider in the province. Their, load centers are located in south of the province, but the power generation plants in the north of the province. Therefore, Manitoba Hydro has to bring generated power to load centers through HVdc power transmission lines over hundreds of kilometers and through difficult undeveloped terrain. To complicate matters, Manitoba faces a harsh winter season with temperatures that go below $-40\,^{\circ}\mathrm{C}$. Currently, Manitoba Hydro uses traditional electric field mills for HVdc power line monitoring which are expensive to acquire, repair and maintain in this context. Less expensive, lower maintenance, robust sensors that consume less power than commercial electric field mills would be highly beneficial.

1.2 dc Electric Field Measurement

Static electric field measurements difficult since dc electric fields do not create cyclic variation over time, so a sensor exposed to a dc electric field charges over time and the measured signal fades out eventually making the measurement inaccurate and unreliable. As a solution to this problem, traditional field mills are constructed in such a way so that an alternating electric field is periodically created by a rotating grounded chopper above the sensor to expose and shield the sensor surface. Figure 1.1 shows a dc field measuring system employing this technique.

However, traditional field mills consume a lot of power, need frequent maintenance due to the wear and tear of their rotating parts, are expensive and are bigger. As a solution, researchers [1, 3–7, 9–12] developed micro electro mechanical

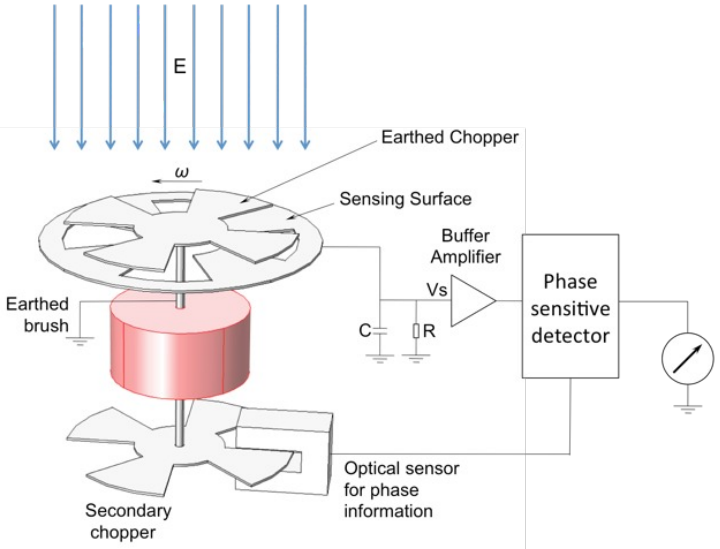

FIGURE 1.1: Schematic of a traditional EFM [1]

.

devices (MEM), which are less expensive, consume less power, are more portable and require less maintenance.

However, the shutters of MEM devices move unexpectedly under high electric fields, which reduces the range of sensor operation. Furthermore, the complex sensor structures increase the fabrication time and cost. Also, some MEM based sensors need higher biased voltages to operate the sensor, thus requiring higher insulation for electronics. Additionally, MEMS design has been limited to lab environment testing only, so MEM sensors that are robust enough to function in field conditions have not been developed yet.

This thesis presents a torsional MEM sensor that actuates using an electric field force. The novel concept in this study is the application of two out- of- phase sinusoidal signals to bias the sensor, causing it to tilt. This tilt can be sensed by the laser and a photo detector system which produces a measurable current, allowing us to measure the tilt of the MEM sensor. Figure 1.2 shows a microscope

image of the fabricated sensor.

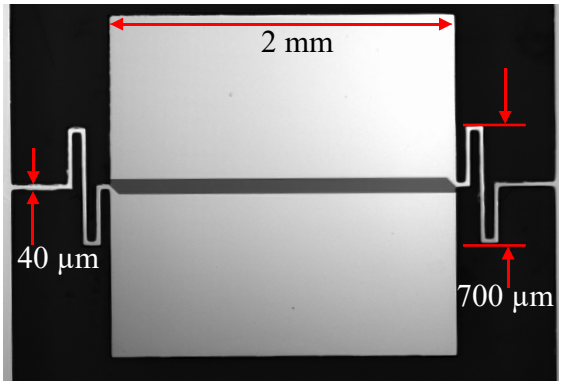

FIGURE 1.2: Microscope image of a fabricated torsional sensor. Up and down electrodes are separated by a SiO_2 insulation layer.

1.3 Research Objectives

The current research objectives are as follows:

1. Design and fabricate a dc electric field sensor that can measure 10's of volts per meter to 100 kilo volts per meter with a linear response using a laser interrogation system.

2. To investigate a low stress fabrication process for the novel micro machined sensors.

3. To develop a reliable on-board electronics and measuring system for the fabricated sensor.

4. To test the fabricated sensor under a mock power line in the presence of corona.

1.4 Document Layout

Chapter 2 will discuss on dc electric field measurement techniques and their advantage and drawbacks. In Chapter 3, new sensor designs, theory behind the sensor operation and sensor simulations using COMSOL multi-physics software will be explained. Chapter 4 will be focused on fabrication including mask designing details, fabrication process, fabrication challenges and solution, and fabricated device measurements. Chapter 5 will be discussed about sensor testing under different environments and results. Finally, Chapter 6 summaries the contribution and concluded with some suggestions for future research.

Chapter 2

dc Electric Field Measurement Techniques

Chapter 1 discussed dc electric field measurements have being used for power industry applications over the decades. Different types of measuring techniques are used by industry to measure dc electric field according to the application. This chapter will discuss the operation principles of some previously reported electric field measuring devices along with their advantages and disadvantages.

Electric field mills, induction probes and electro optic meters are the most common mechanisms for electric field strength measurements. All these sensors belong to non-contact dc electric field sensors category. In recent years, the interest in research about micro machined electric field sensors increased significantly [13]. These miniaturized devices use the same measurement techniques as the ordinary devices while being smaller and low-cost for manufacturing.

2.1 Electro-Optic meters

The working principle of electro-Optic meters is based on changing material optical properties according to an incident electric field. When an electric field is incident upon an electro-optic medium the birefringent properties of that medium change. This can result in a change of the direction of light propagation through the crystal. The change can be measured by using a variety of optical system architectures [14]. For this type of sensor, no ground reference is needed unlike induction probes and field mills. Electric field optical sensors are generally based on linear electro-optic effect. The speed of light in a material is defined by its refractive index. Equation 2.1 [15] shows refractive index for each orthogonal component:

$$n = n_0 + aE + bE^2 + ... \tag{2.1}$$

where n is the refractive index of the material, n_0 is the normal refractive index when there is no electric field (E), a is the coefficient of Pockels effect, and b is the Kerr effect coefficient. Higher order of E has less effect on the n and therefore can be neglected.

2.2 Induction Probe or Surface Probe

The basic principle of the induction probe technique is to expose a metal plate under a local electric field and measure the accumulated charge in the metal plate, as shown in theFigure 2.1. The amount of charge on the induction plate can be calculated by Gauss's law. For a plate of area A, the magnitude of charge Q

induced by an electric field E is given by,

$$Q = \varepsilon_r \varepsilon_0 EA \qquad [\text{C}] \quad (2.2)$$

where, $\varepsilon_r \sim 1$

When the induction plate is connected to a capacitor, the voltage across the capacitor plates can be calculated as,

$$V_m = \frac{Q}{C} = \frac{\varepsilon_0 EA}{C} \qquad [\text{V}] \quad (2.3)$$

Surface probes or induction probes can be used to measure electric fields at different distances by adjusting the reading for the new distance. This technique is valid only for a charge free or a corona free environment. This sensor type is not suitable to measure electric fields under dc power lines, since space charges can travel with the wind [16] and be deposited on the induction plate resulting an incorrect voltage reading. Therefore, this method requires frequent zeroing and shielded conditions, resulting in longer measurement times.

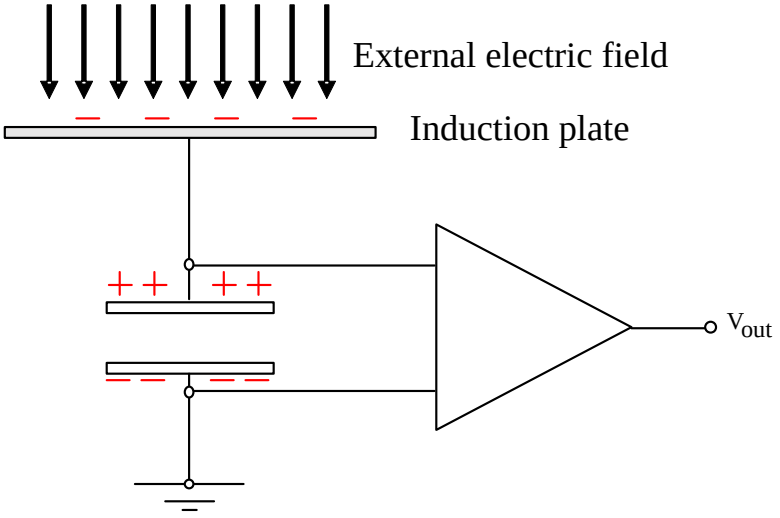

FIGURE 2.1: Induction probe principle.

2.3 Electric Field Mills (EFMs)

Electric field mills have been commercially used for atmospheric sciences and measuring electric fields under HVdc lines for more than two decades [9].

2.3.1 Operating principle

In these type of devices, a mock ac field is created by rotating a shutter exposing and shielding the sensor plate as shown in theFigure 2.2. Rotation is done by a mechanical motor. Exposure results in electrode charging and shielding results in discharging. This process leads to minimization of effects from ironic charges which will cause errors in the measurements. This process does not suffer from the frequent zeroing problem faced in induction probe technique and it also has higher sensitivity compared to induction probe systems. But these field mills are more complex and more expensive than induction probe systems.

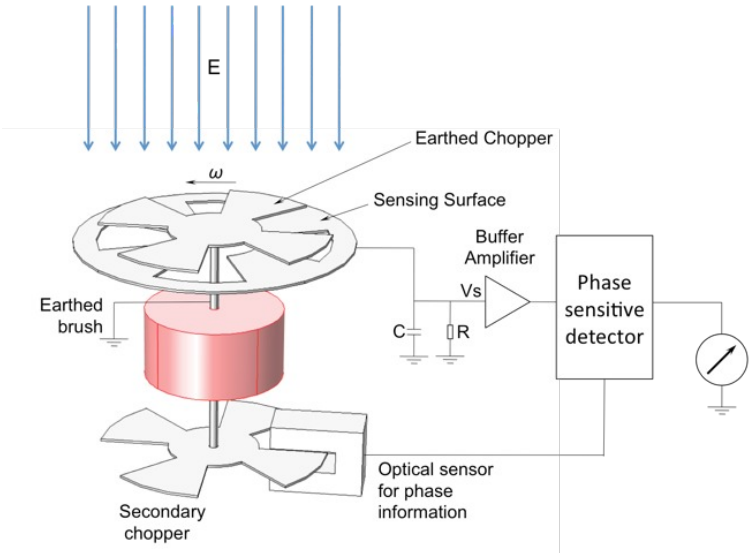

Yu Zhou. Investigation of a Micromachined Electric Field Mill to Maximize the Electrostatic Field Sensitivity. Department of Electrical and Computer Engineering, University of Manitoba, Winnipeg, Manitoba, 2011.

FIGURE 2.2: Schematic of a traditional EFM [1]

.

2.4 Cylindrical mill/ Free body meter

This type of field mill uses the same principle as the previous field mills but only measures the electric field perpendicular to the cylinder as other directional field components cancel out. Using three orthogonal electric field mills, the direction of the electric field can be determined. Figure 2.3 shows an example of a free body meter.

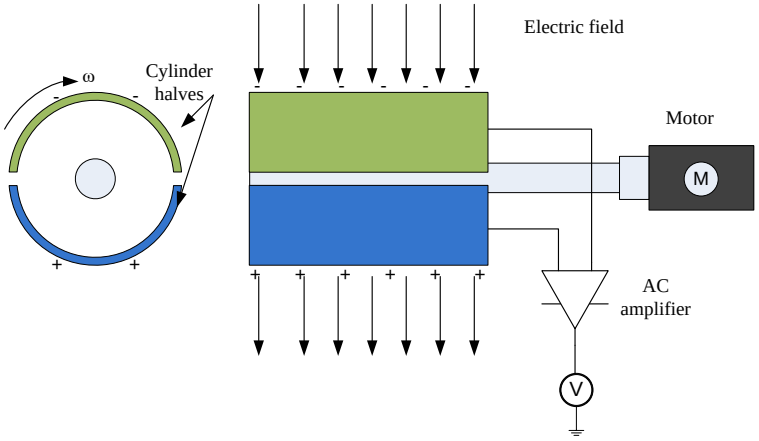

FIGURE 2.3: Schematic of a cylindrical field mill.

It has a rotating cylinder with two halves connecting through a low impedance wire. When one side is exposed to electric field, that side is polarized as negative and through the low impedance wire other side is polarized as positive. As the cylinder rotates polarity of of the cylinder halves changes and it creates a mock ac current in the connecting wire. The ac current created by electric field is equal to Equation 2.4 [1, 17],

$$I = 3\omega\pi R^2 \varepsilon_0 E \sin(\omega t) \quad \text{[A]} \quad (2.4)$$

where R is the radius of the cylinder rotating at an angular frequency ω, and E is the incident electric field. According to Equation 2.4, the generated current

magnitude is proportional to the electric field.

Renno et al. [10] presented a free body meter which was 2.2 cm diameter and 15 cm long.

2.5 Micromachined (MEMS) electric field sensors

Micromachined electric field sensors are manufactured by semiconductor fabrication techniques, which can reduce the power consumption compared to existing field mills, production cost and maintenance issues. Since the ability to make smaller devices is possible, many sensors can be used for the same measurement and increase the reliability.

Similar to conventional electric field mills, MEMS electric field mills have a moving shutter, sensing electrodes and a driving system. The main difference between the two is in the shutter structure. The conventional field mill has a rotational shutter, whereas, in MEMS field mills it has been replaced by a vibrating shutter. Comb drive actuated shutters are a popular actuating mechanism for micro-machined electric field mills (MEFM). For further information about the comb drive mechanism, refer to Chapter 3 of [9].

Figure 2.4 shows the principle behind a MEMS field mill sensor developed by Wijeweera et al. [2, 9]. When the shutter moves the bottom electrodes are exposed or shielded to the incident electric field . This creates an ac current on the bottom electrodes. The magnitude of generated ac current is proportional to the incident electric field. Equation 2.5 defines the relationship between the magnitude of the generated current in the presence of the electric field,

$$i_{out} = \varepsilon_0 E_n \frac{dA}{dt} \qquad \text{[A]} \quad (2.5)$$

where ε_0 is the permittivity of free space, E_n is the component of the electric field normal to the electrodes, and A is the effective area of the electrodes.

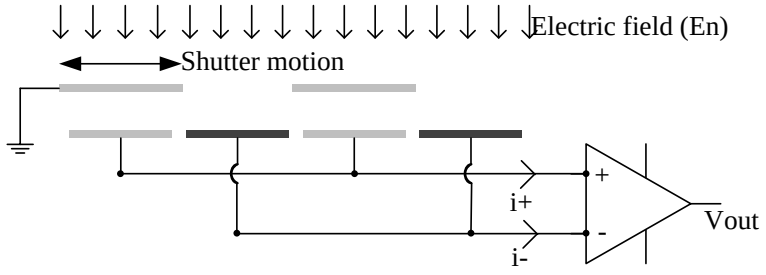

FIGURE 2.4: Operating principle of a micro-machined field mill.

Figure 2.5 shows a set of electrodes on the left side that are visible through the shutter openings (yellow colour). When the shutter moves horizontally, these electrodes will be covered, while the other set of electrodes on the right side will be exposed to the electric field.

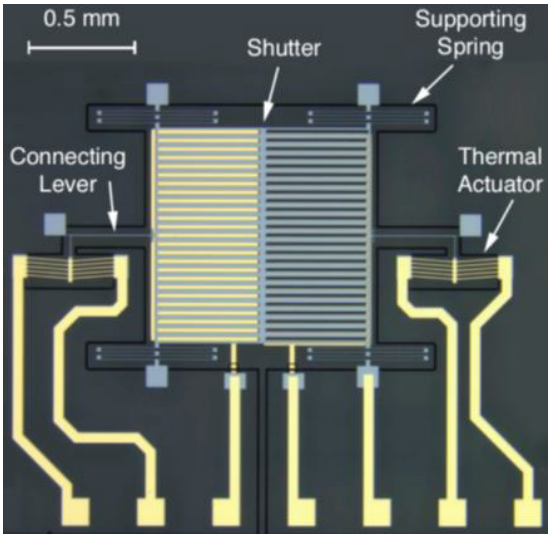

B. Bahreyni, G. Wijeweera, C. Shafai, and A. Rajapakse. Analysis and design of a micromachined electric-field sensor. Journal of Microelectromechanical Systems,

FIGURE 2.5: Microscope photograph of thermally actuated comb drive developed by Wijeweera et al. [2]

Horenstein et al. [3] developed a MEFM system as shown inFigure 2.6 and shutter was actuated by a comb drive. The shutter has a 10 μm $\times$ 10 μm aperture and with shutter movement the electrode is exposed to the incident electric field. The disadvantage with this sensor is it requires 60 V to operate, which is considered as a higher operating voltage for a MEMS sensor. Furthermore, this high voltage will interfere with the measurement.

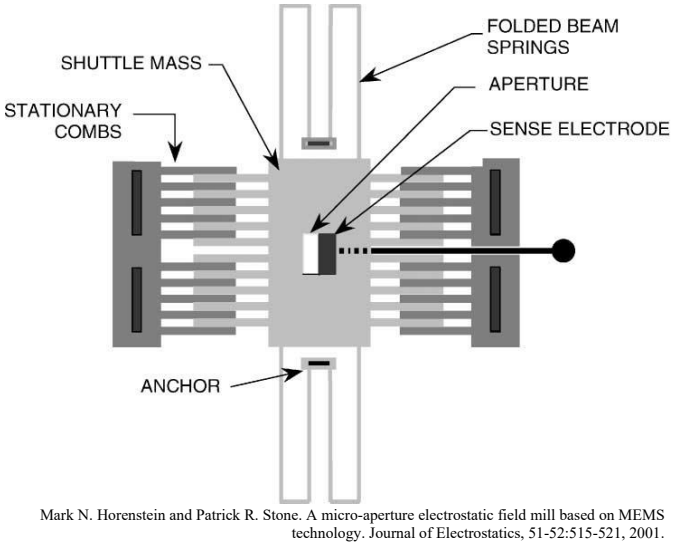

FIGURE 2.6: Schematic of MEFM developed by Horenstein et al. [3]

2.5.1 Vertically moving shutter sensor with Piezoelectric actuation

There are a few Piezoelectric electric field sensors reported in the literature. Similarly to field mill systems, Piezoelectric actuated electric field sensors use the induction probe principle following Gauss' Law.

In this work lead-zirconate-titanate (PZT) actuators are used for achieving a large displacement (10 μm). As seen in Figure 2.7, the green screen moves up and down resulting shielding and exposing of pillar electrodes as shown in blue.

When the screen is in the top position, electric field trough the holes can not reach the underneath pillar electrodes. This prevents the charging of the floating sensor electrodes. When the screen is in the bottom position , the electrodes are exposed to incident electric field. Floating electrode charge is measured by sending sensor output through a current to voltage converter circuit.

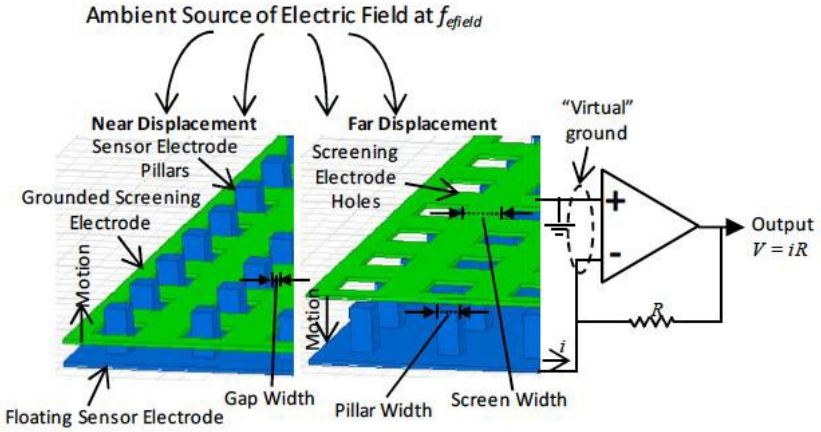

S. Ghionea, G. Smith, J. Pulskamp, S. Bedair, C. Meyer, and D. Hull. MEMS electric-field sensor with lead zirconate titanate (pzt)-actuated electrodes. In 2013 IEEE SENSORS, pages 1-4, Nov 2013.

FIGURE 2.7: Piezoelectric actuated electric field sensor developed by Ghionea et al. [4]

2.6 Electrostatic force based MEM sensors

The basic operation principle is electro static field force created by an external electric field source, which pulls the light weight metallized membrane towards to the field source which is supported by micro springs. The sensor displacement can be measured by either capacitively or by a laser employed system. Figure 2.8 shows an example of an electrostatic force based MEM sensor. The voltage difference between the upper electrode (V_{DC}) and the sensing electrode (metallized membrane) creates a electric field force that pulls the sensing electrode upwards. The force on the sensing electrode is given by Equation 2.6 assuming parallel plate capacitor geometry.

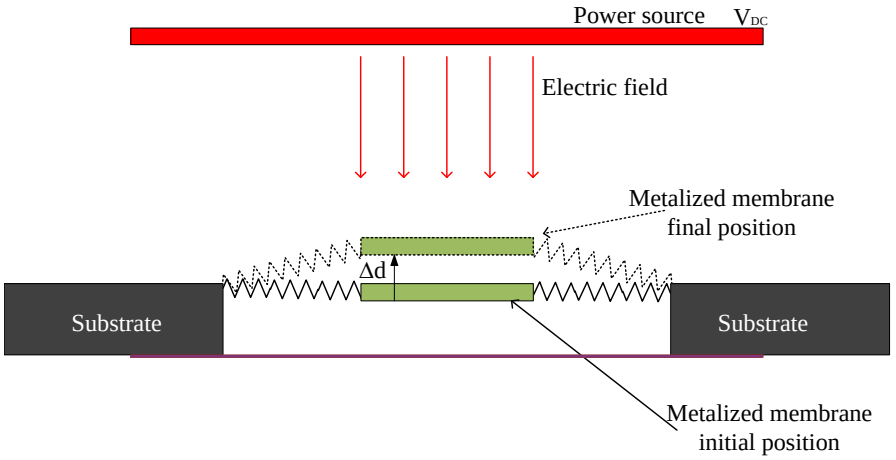

FIGURE 2.8: The principle of electrostatic force based MEM sensor.

$$F_e = \frac{1}{2}\varepsilon_0 A E^2 = \frac{1}{2}\varepsilon_0 A\left(\frac{(V_{DC} - V_m)^2}{z^2}\right) \quad [\text{N}] \quad (2.6)$$

where F_e is the electrostatic force on the membrane, ε_0 is the permittivity of vacuum, A is the membrane surface area, E is electric field, z is the distance between upper and bottom electrodes, V_{DC} is the voltage of the field source and V_m is the voltage on the membrane.

The mechanical restoring force on the springs can be written as Equation 2.7,

$$F_m = -k\Delta d \quad [\text{N}] \quad (2.7)$$

where F_m is the restoring mechanical force, k is the total spring constant of the suspended springs, and Δd is the membrane displacement.

2.6.1 Capacitive interrogation

Figure 2.9 shows a sensor developed by Chen et al.[5] using the electrostatic force principle. In his work, electric field strength is measured capacitively. This system consists of two electrodes. The spring suspended membrane is connected to the ground and the bottom electrode is at floating potential creating a voltage difference between the two electrodes. Electric field force pulls the membrane towards to the power source changing the distance between the two electrodes. This creates a change in capacitance C_m, which is measured.

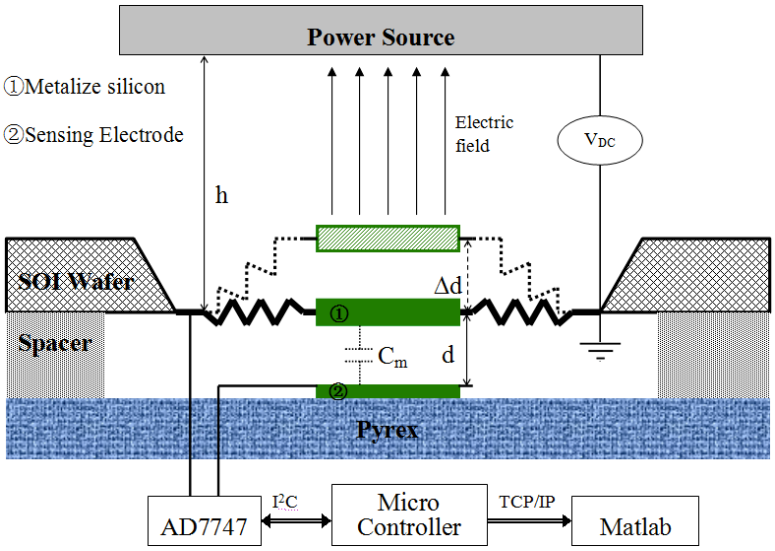

Tao Chen. MEM electric field sensor using force detection with capacitance interrogation. In 2013 IEEE Power Energy Society General Meeting, pages 1-4, July 2013.

FIGURE 2.9: Electrostic force based capacitive interrogation method developed by Chen et al. [5]

This result can be expressed by the Equation 2.8 assuming the parallel plate capacitor model,

$$\Delta C = \frac{C_{mi}^2}{\frac{2k}{E^2} + C_{mi}} \quad [\mathrm{C}] \qquad (2.8)$$

This sensor showed sensitivity of 16 kV/m. The disadvantage with this system is the non-linear relationship of ΔC with the incident electric field, and also a reference ground is needed [5].

2.6.2 Laser interrogation

Figure 2.10 shows an electrostatic force based sensor monitored by a laser interrogated system. When an electric field is present, the membrane lifts and beam position of the reflected laser beam moves into a different position on the surface of the photodetector. The laser displacement is measured electronically determine the strength of the electric field. Roncin et al. [6] showed a resolution of 5 kV/m under a dc field, and a 0.3 V/m resolution under an ac field at 97 Hz.

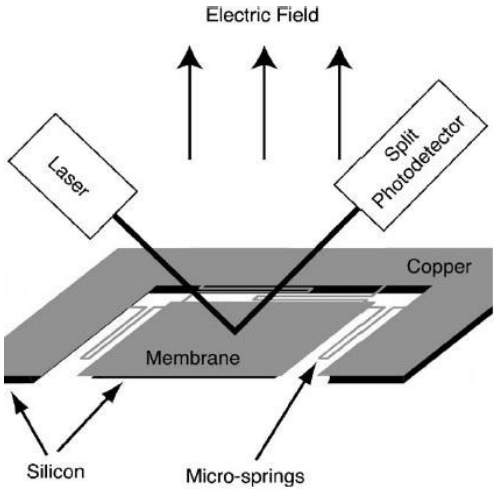

A. Roncin, C. Shafai, and D.R. Swatek. Electric field sensor using electrostatic force deflection of a micro-spring supported membrane. Sensors and Actuators A: Physical, 123-124:179 -184, 2005.

FIGURE 2.10: Schematic of sensor developed by Roncin et al. [6] used to measure deflection of membrane.

The sensor operating principle can be derived by a dc - ac capacitor model. The dc voltage acts as the electric field source and an ac voltage is used to bias the sensor.

In his work, the sensor was operated using an ac bias signal at the resonance frequency. Equation 2.6 can then be modified as Equation 2.9,

$$F = -\frac{\varepsilon_0 A}{2z^2} \cdot (V_{DC}^2 - 2V_{DC}V_m \sin(\omega t) + V_m^2 \sin^2(\omega t)) \tag{2.9}$$

The second term on the right of the Equation is the modulated electric field. This can be monitored by the sensor electronics.

Figure 2.11 shows another electrostatic force based sensor developed by Chen et al. [7], measurements 75 cm under a 20 kV simulated power line demonstrated a resolution of 17 V/m and sensitivity of 360 mV/(kV/m).

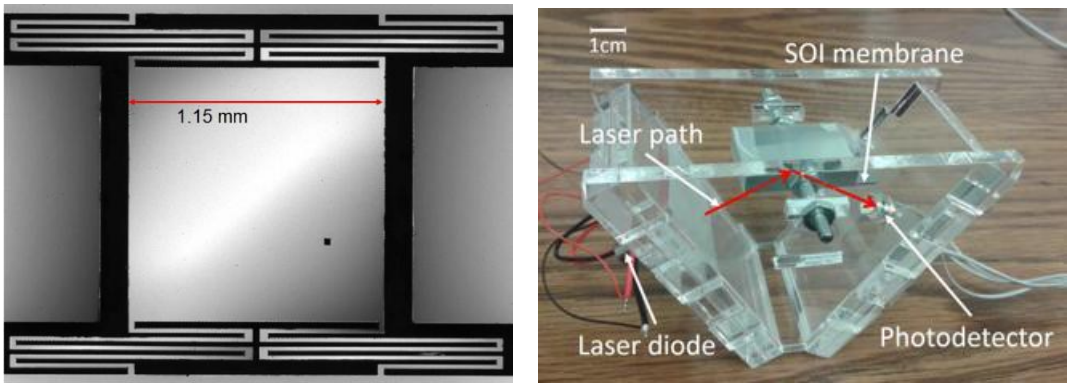

T. Chen, C. Shafai, A. Rajapakse, J.S.H. Liyanage, and T.D. Neusitzer. Micromachined ac/dc electric field sensor with modulated sensitivity. Sensors and Actuators A: Physical, 245:76-84, 2016.

FIGURE 2.11: (a) *SOI* membrane based sensor developed by Chen et al. (b) Acrylic frame design consist of sensor, laser and photo detector used to measure sensor response. [7]

In my work, laser interrogation technique is used to measure the displacement of the torsional sensor designs. Major discussion of this topic is reserved for Section 3.2.

2.7 Performance Comparison

Table 2.1 compares the sensor types discussed in this Chapter.

TABLE 2.1: Comparison of different electric field sensors

Reference by year	Sensor type	Actuation mechanism	Sensitivity	Advantage and Disadvantages
I. Zaldivar-Huerta et al. 2004 [18]	Electro-Optic	Electro-Optic properties		Less disturbance to measured electric field, less sensitivity, only ac
A. Roncin et al. 2005 [6]	MEMS electrostatic force	Electrostatic force and laser interrogation	5kV/m –dc 0.3 V/m - ac	High sensitivity for ac at resonant frequency
Wijeweera et al. 2009 [2]	MEFM	Thermally actuated	42 V/m	High sensitivity at resonant
Johansson et al. 2010 [19]	Free-body meter	Two rotating surfaces connected with low impedance conductor	100 V/m	No ground reference required
Yang et al. 2011 [20]	MEFM	Comb drive actuated, comb-shape electrodes applied	∼40 V/m	High sensitivity, operating at resonance
Chen et al. 2013 [5]	MEMS	Electrostatic force and capacitive interrogation	16.2 kV/m.	Low resolution, non linear relationship
Kobayashi et al. 2013 [21]	MEMS	Self resonance and PZT Induction probe	-3 to 3kV range	Complexity with fabrication
Ghionea et al. 2014 [4]	MEFM	PZT actuation Induction probe	0.19 V/m/rtHz in vacuum (0.30 V/m/rtHz in air)	AC only, low driving voltage, frequency modulation, complexity with fabrication
Chen et al. 2016 [7]	MEMS	Electrostatic force and laser interrogation	180 mV/(V/m)	High sensitivity ac and dc

Chapter 3

Sensor Design and Theory

This chapter discusses the sensor designs and the electrostatic theory behind the sensor.

3.1 Sensor Design

Figure 3.1 shows the basic design of the torsional micro-mirror sensor. This symmetrical sensor comprises of a silicon (Si) mirror platform suspended by two silicon micro springs. The mirror platform size is 2 mm $\times$ 2 mm and the springs are 40 μm wide. The entire film structure and springs are made of single crystal Si and the ends of the springs are attached to the silicon substrate. The sensor and spring thicknesses are selected as 10 μm for convenient fabrication.

Figure 3.2 shows three different torsional micro-mirror designs with different spring lengths. The length of the spring determines the sensor resonance frequency. This sensor has two aluminium electrodes on the sensor surface (Figure 3.1). These electrodes are biased with opposite polarity ac voltages with the same magnitude

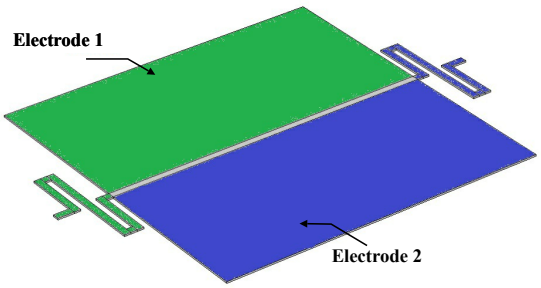

FIGURE 3.1: Basic torsional mirror (two spring) sensor design.

and therefore the sensor can operate without a reference ground. Furthermore, this configuration creates two different electrostatic forces on the two electrodes and rotate the sensor mirror platform around its symmetrical axis.

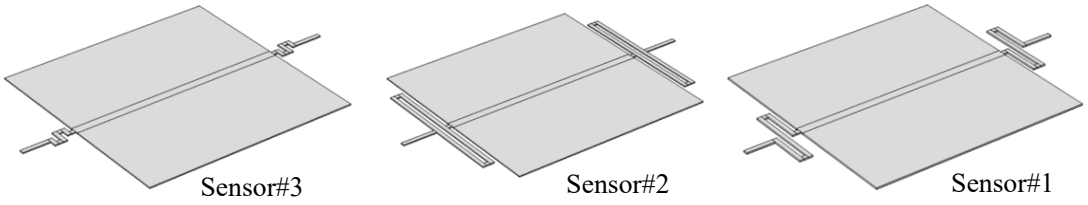

FIGURE 3.2: Torsional mirror sensor designs.

The term "Sensor#X" will be used throughout this thesis to discuss specific details relevant to the particular sensor.

3.2 Electrostatic theory

The forces on the sensor electrodes can be explained using a parallel plate capacitor system shown in Figure 3.3. Here, electric field (E) between upper and lower electrodes are given by,

$$E = \frac{V}{d} \qquad [\mathrm{Vm}^{-1}] \quad (3.1)$$

where V is the voltage difference between two plates and d is the distance between the plates.

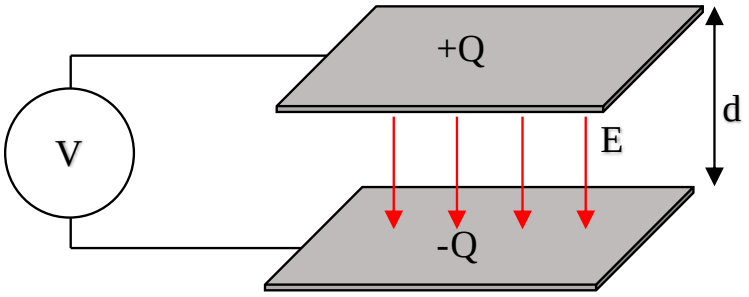

FIGURE 3.3: Parallel plate capacitor system.

The energy stored in a parallel plate capacitor (W) is given by,

$$W = \frac{1}{2}CV^2 = \frac{1}{2}\frac{\varepsilon_0\varepsilon_r A}{d} \times (E \cdot d)^2. \qquad [\text{kg m}^2\ \text{s}^{-3}] \quad (3.2)$$

where, A is the area of the capacitor, ε_r is the relative permittivity of the material and ε_0 is permittivity of the free space. The force between two parallel plates can be written by,

$$F = -\nabla W = -\frac{1}{2}\varepsilon_0\varepsilon_r A E^2 \qquad [\text{N}] \quad (3.3)$$

where $-\nabla W$ is the negative gradient of the work energy.

Figure 3.4 shows the sensor in the presence of a dc electric field. The external voltage source (V_{dc}) and the sensor bias voltage (V_{ac}) create a voltage difference and hence, an electric field is created between two potentials.

With V_{dc} being a positive voltage, the positive sensor electrode ($+V_{ac}$) will experience less attraction force than the negatively biased sensor electrode ($-V_{ac}$). This leads the sensor to torsionally tilt around its axis of symmetry. The tilt of the sensor can be monitored by sensor electronics, which is explained in Chapter 5.

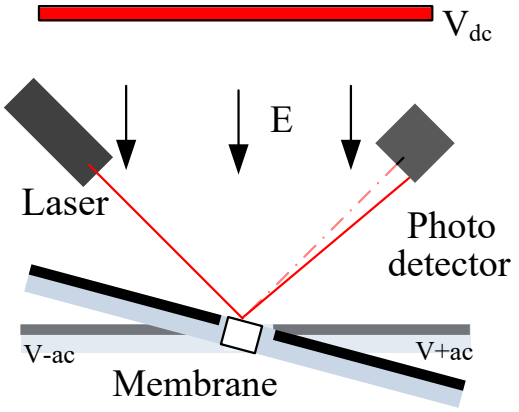

FIGURE 3.4: Sensor working principle.

The expression in 3.4 is derived by neglecting the fringing fields and assuming the electric field generated between source and the mirror platform is uniform. Electrostatic force between two of the capacitor plates with the potential V_{dc} and V_m is given by,

$$F = -\frac{1}{2} \cdot \varepsilon_0 \varepsilon_r A \left(\frac{V_{dc} - V_m}{d}\right)^2 \qquad [\text{kg·ms}^{-2}] \quad (3.4)$$

By substituting $V_m = V_{ac} \sin(\omega t)$ in 3.4,

$$F = -\frac{1}{2} \cdot \varepsilon_0 \varepsilon_r A \left(\frac{V_{dc} - V_{ac} \sin(\omega t)}{d}\right)^2 \qquad [\text{kg·ms}^{-2}] \quad (3.5)$$

Equation 3.6 is written by expanding 3.5.

$$F = -\frac{\varepsilon_0 \varepsilon_r A}{2d^2} \cdot (V_{dc}^2 - 2V_{dc}V_{ac} \sin(\omega t) + V_{ac}^2 \sin^2(\omega t)) \quad (3.6)$$

Three frequency components are contributing to the electrostatic force, according to the Equation 3.6.

- V_{dc}^2 corresponds to dc component,
- $2V_{dc}V_{ac} \sin(\omega t)$ corresponds to fundamental frequency component, and

- $V_{ac}^2 \sin(\omega t)^2$ corresponds to 2^{nd} harmonic.

The dc component and the 2^{nd} harmonic of the fundamental frequency component have non-linear relationship with the electrostatic force F. The center term (which is the modulated signal formed by V_{dc} and V_{ac}) has a linear relationship with the electrostatic force F. This term can be written as,

$$F = \frac{\varepsilon_0 \varepsilon_r A}{d^2} \cdot (V_{dc} V_{ac} \sin(\omega t)) \qquad [\text{kg}\cdot\text{ms}^{-2}] \quad (3.7)$$

3.3 COMSOL Multiphysics software simulations

The torsional micro mirror design has mainly two kinds of mechanical movements due to an incident electric field. First, the resultant electrostatic force on the electrodes, moves the mirror platform vertically up. Second, since the force on the electrodes is not equal, differential force results in a torsional tilt of the mirror platform around its symmetrical axis.

Due to the complexity in the spring arrangement, calculation of the spring constant for torsional motion is difficult. To study the sensor behaviour, simulations using COMSOL Multiphysics software[1] were performed with changing parameters such as spring length, thickness and width. Here, the thickness of mirror platform was maintained at 10 μm (mass is a constant).

The objective of the research is to design sensors that have frequency between 500 Hz to 2 kHz.

[1]COMSOL Multiphysics software uses finite element analysis technique for solving multiphysics problems.

3.3.1 Simulation in the presence of a dc field

Figure 3.5 shows the COMSOL simulation set-up where the sensor designs were simulated inside an air box. The top side of the air box acts as the source voltage (to create the electric field) and the bottom side of box acts as the ground. This creates a uniform electric field inside the air box. The sensor is positioned in the centre of the air box.

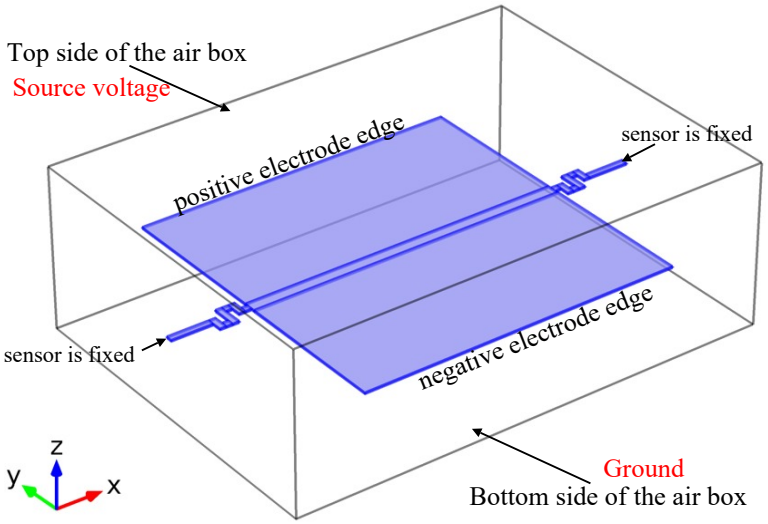

FIGURE 3.5: COMSOL simulation setup.

Sensors were studied with stationary analysis module to see sensor deflection under different electric field conditions. Opposite dc voltage is applied with same magnitude to sensor electrodes (bias voltages) and a positive electric field is created by applying a voltage to the top side of the air box.

Figure 3.6 shows sensor#3 vertical displacement with 0 V bias to the sensor. It can be seen that the sensor moves up without creating a tilt. Arrows show the direction of the electric field force.

Figure 3.7 shows sensor#3 displacement for a 200 kV/m electric field when the source at 10 V and the sensor is biased at 1 V. The positive electrode (Electrode

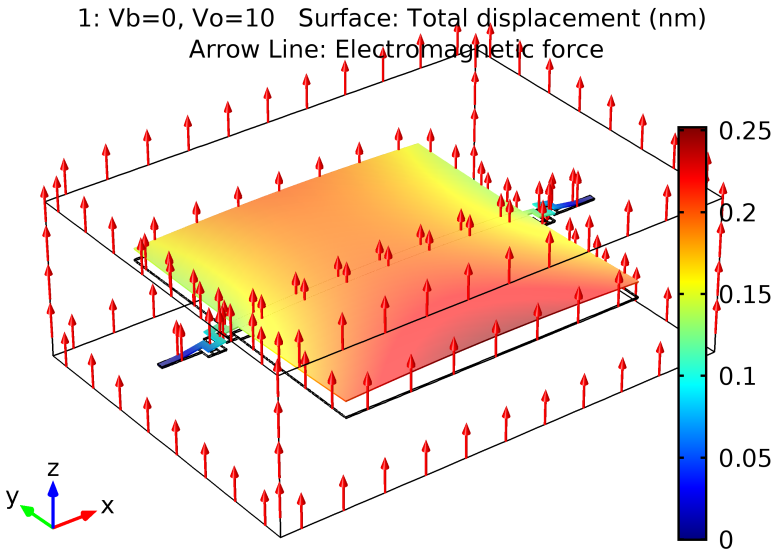

FIGURE 3.6: Sensor#3 vertical displacement with 0 V bias.

1) is in y direction and the negative electrode (Electrode 2) in the $-y$ direction. Arrow lines indicate the electromagnetic force direction. It can be seen that sensor has a vertically up displacement and a tilt in counter clockwise. Vertical displacement is due to the resultant electric field force on the mirror platform and the tilt is caused by the differential forces on the electrodes.

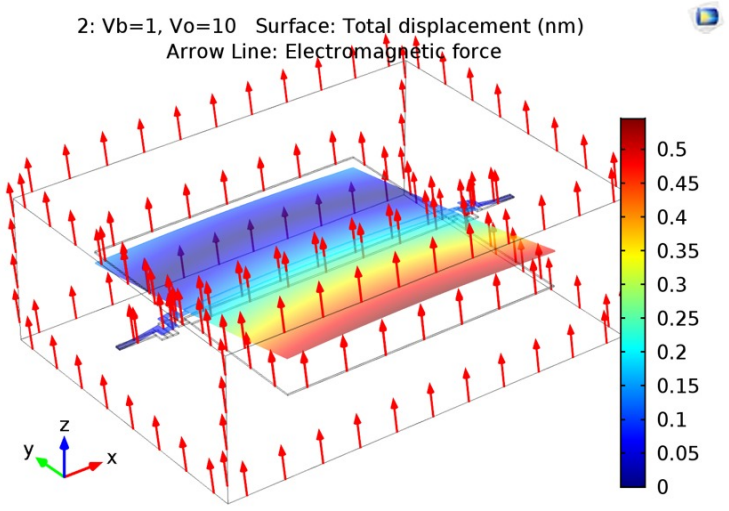

FIGURE 3.7: Sensor#3 response under a 200 kV/m electric field.

Membrane deformation of the sensor was measured by applying different electric fields.Figure 3.8 shows Sensor#3 response for different electric fields. Sensor displacement was measured across the center of the sensor surface by placing a line bisecting the material. It can be seen that positively biased electrode side (Electrode 1) has a lower displacement and negatively biased electrode side (Electrode 2) has a higher displacement. Further, it can be noted that sensor surface displacement is not linear in Figure 3.8. This is due to the attractive electric field force between opposite polarity electrodes on the mirror platform.

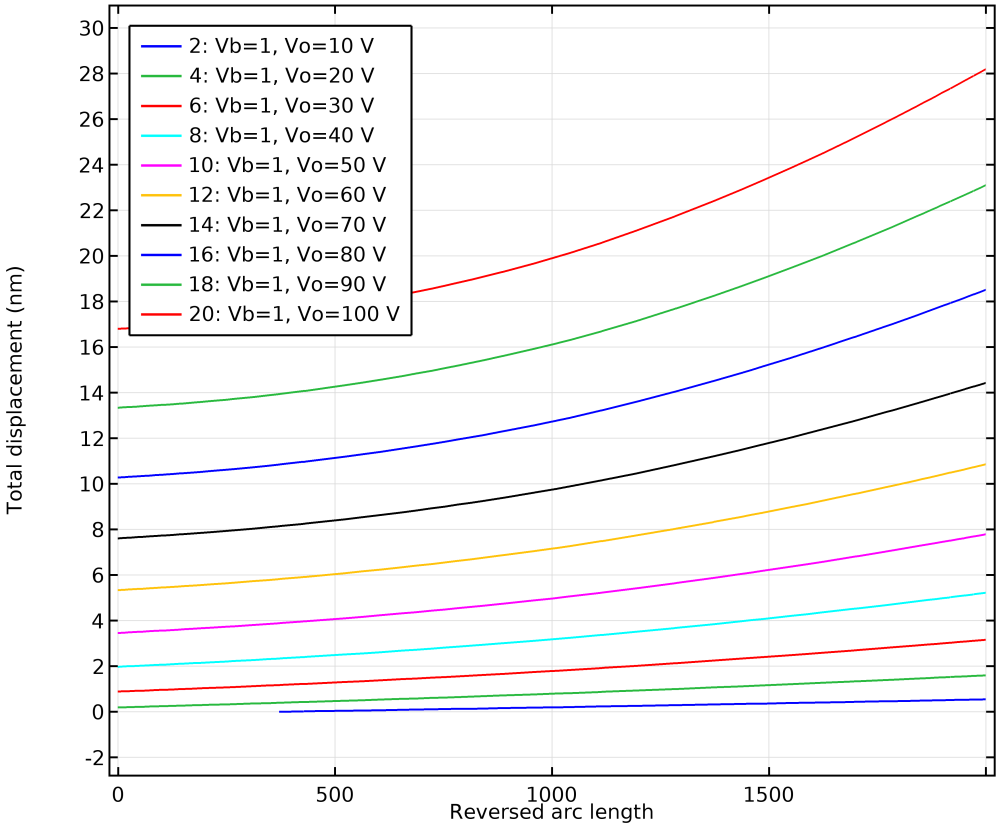

FIGURE 3.8: Sensor#3 displacement with applied source voltage.

Figure 3.9 shows positive and negative electrode edge (see Figure 3.5) displacements under different source voltages. It can be seen that when the source voltage increases negative electrode edge displacement increases than the positive electrode edge. This phenomena proves that the tilt angle is increasing. The electrode displacement is in the nanometre range and the tilt angles is very small. This helps to keep effective incident electric field area of the mirror platform as a constant (Equation 3.7). Another observation from the Figure 3.9 is that the electrode edge displacement is not linear. This is due to non-linear relationship of the electrostatic force with the electric field (see Equation 3.3).

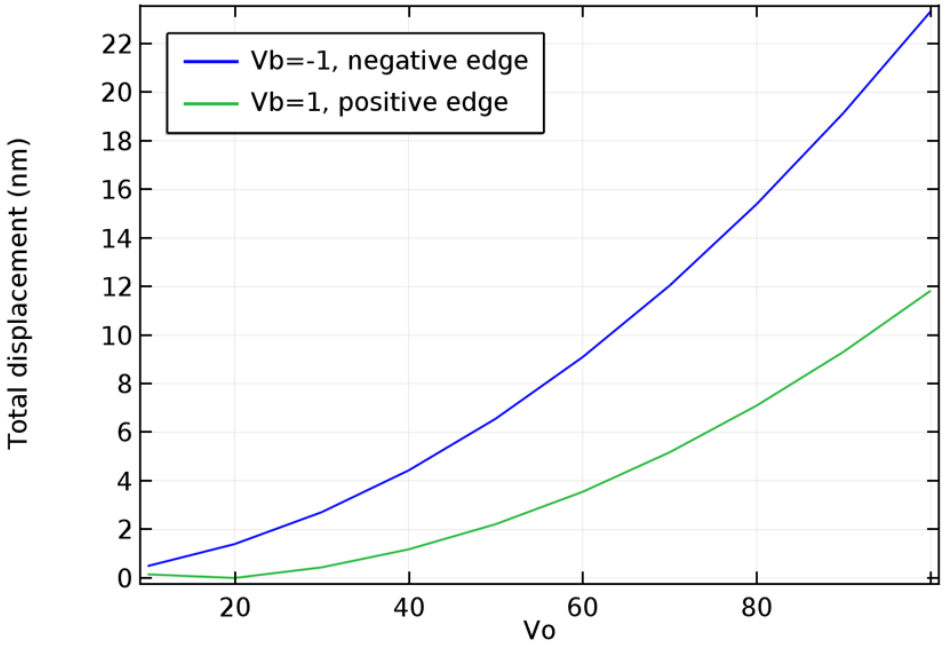

FIGURE 3.9: Sensor#3, electrode edge displacement.

3.3.2 Resonance frequency analysis

For all the sensor types, the first eigen frequency (mode 1) was considered as the operating frequency. For this, two spring structures show the torsional motion around the x axis (symmetric axis). Figure 3.10 shows the motion at it's 1^{st} eigen frequency (mode 1).

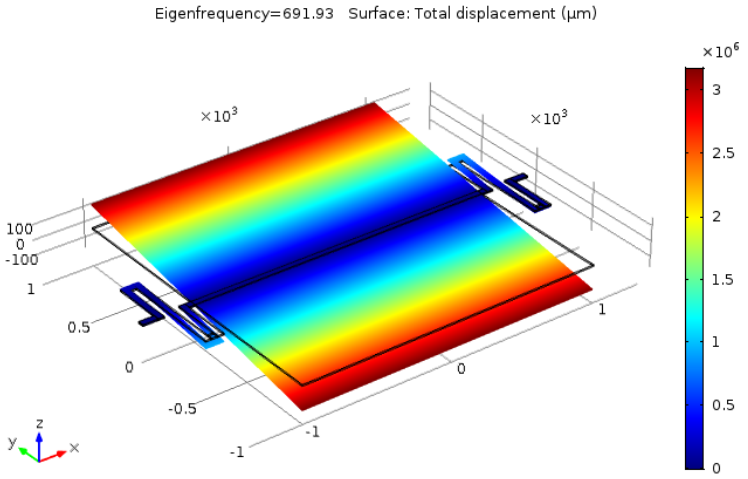

FIGURE 3.10: First Eigen frequency behaviour of a torsional sensor.

The thickness of the mirror platform is maintained at 10 μm during the simulations. Figure 3.11 shows the variable sensor parameters used for the study.

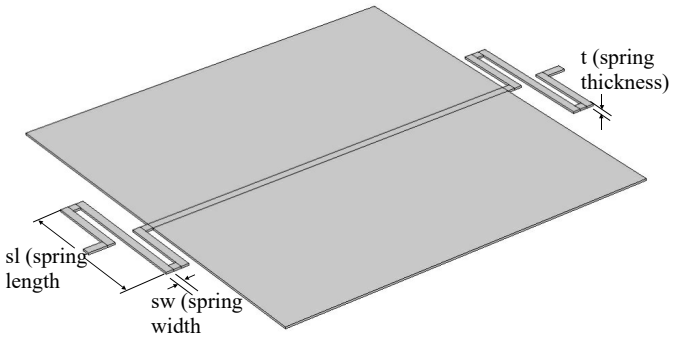

FIGURE 3.11: Torsional sensor's variable parameters for eigen frequency study.

Figure 3.12 shows the first eigen frequency change with different spring thickness for different spring widths. It can be seen that with increasing spring thickness the resonance frequency increases linearly.

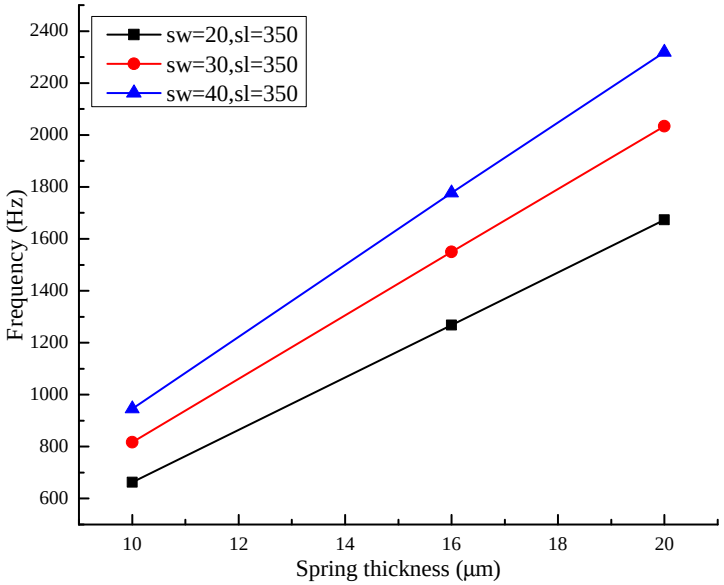

FIGURE 3.12: The first eigen frequency change with spring thickness for different spring widths.

Figure 3.13 shows the resonance frequency change in torsional model with respect spring length. When the spring length increases resonance frequency reduces.

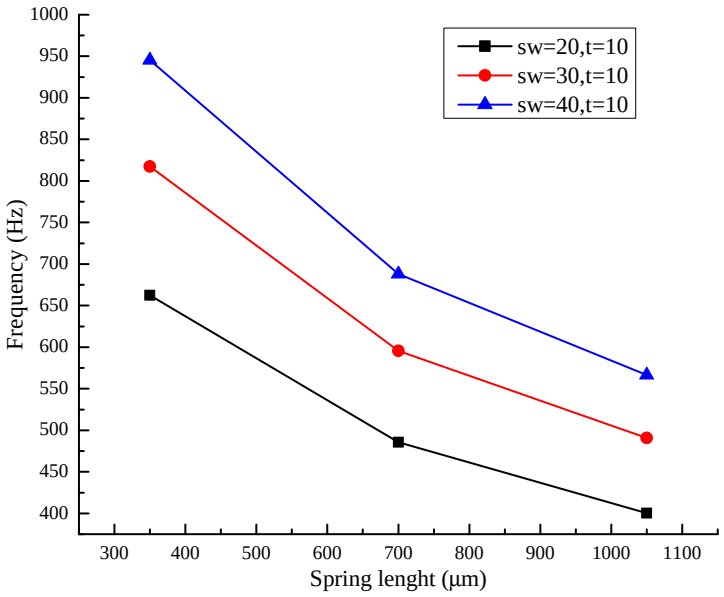

FIGURE 3.13: The first eigen frequency change with spring width for different spring lengths.

Figure 3.14 shows the resonance frequency change in torsional model with respect to spring width. When the spring width increases resonance frequency increases.

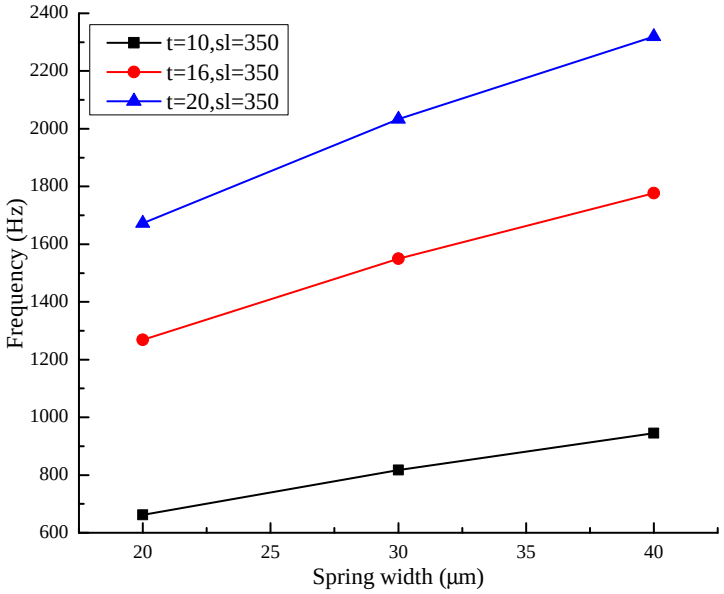

FIGURE 3.14: The first eigen frequency change with spring length for different spring widths.

Table 3.1 shows frequency responses for different parameters for torsional sensor design simulations. This information was used for sensors' frequency selection. It can be concluded that, when spring length increases frequency reduces. When the spring thickness and the spring width is increased, resonance frequency increases.

TABLE 3.1: Sensor resonance frequency with physical parameters.

Spring width (μm)	Thickness (μm)	Spring length (μm)	Frequency (Hz)
20	10	350	662
20	10	700	486
20	10	1050	400
20	16	350	1268
20	16	700	951
20	16	1050	792
20	20	350	1673
20	20	700	1286
20	20	1050	1081
30	10	350	817
30	10	700	595
30	10	1050	491
30	16	350	1550
30	16	700	1164
30	16	1050	969
30	20	350	2034
30	20	700	1564
30	20	1050	1318
40	10	350	945
40	10	700	688
40	10	1050	566
40	16	350	1777
40	16	700	1338
40	16	1050	1114
40	20	350	2319
40	20	700	1789
40	20	1050	1513

Chapter 4

Sensor Fabrication

This chapter describes different stages of the device fabrication process from mask design to final device prototype.

Section 4.1 offers a detailed explanation of prior preparation for the sensor fabrication process with material and process selection. Section 4.2 briefly explains the successful fabrication technique along with detailed process parameters. Section 4.3 discusses the sensor's physical dimensions after the completed fabrication. Section 4.4 gives a detailed explanation of procedures and fabrication recipes taken to overcome intrinsic material stress. Section 4.5 explains, initial fabrication trials, that were carried out to overcome fabrication challenges.

4.1 Mask Design for Sensor Fabrication

In this stage, it is required to determine materials to be used in the fabrication process, fabrication limits, and calculate how many masks will be needed for successful sensor fabrication. In order to clarify the final product of the fabrication,

Figure 4.1 shows the expected sensor design with selected materials. Please note, the shown spring structure is different than the fabricated spring structure.

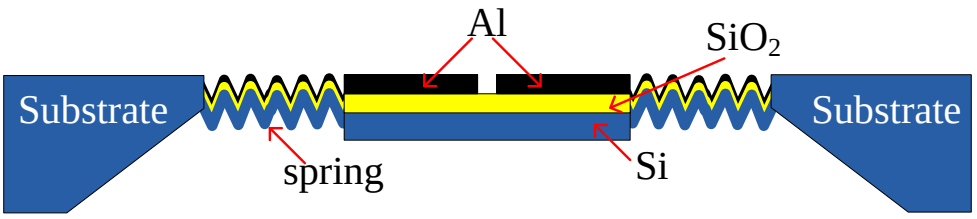

FIGURE 4.1: Sketch of the sensor with different material layers.

4.1.1 Material and process selection

The final sensor should bounce a laser beam at the centre of the mirror platform. Therefore, the outer layer of the sensor must be a smooth metal surface. Initially, Copper (Cu), Al, Gold (Au) were considered and the pros and cons of each material were analyzed.

All are excellent conductors, but, in nature, Cu does not reflect light efficiently and it requires another adhesive layer deposited between Si and Cu. Au is expensive and also requires an adhesion layer. Al is a good reflector and it is economical, so it was selected as the sensor metal layer. However, when two bias voltages are applied on top of the sensor it short circuits because Si is a semiconductor. Therefore, an insulation layer on the Si wafer was needed to separate the Al from the Si. Si_3N_4 and SiO_2 were possible options for insulation, but SiO_2 was selected as the insulator, since we had sputtering and wet oxidation processes for it.

4.1.2 Layer-wise mask development

According to the Section 4.1.1, two materials have to be deposited on Si. As they have two different patterns two masks will be needed. Furthermore, according to Figure 4.1 there is a cavity under the mirror platform and springs. Therefore, another mask was needed to create the back cavity on the silicon substrate. Tanner Suite software was used to design the lithography masks of the selected sensor types.

Figure 4.2 shows the mask usage during the different fabrication stages. It can be seen how different designs have used in the fabrication process. For each mask design, mask dimensions were calculated according to process parameters and it is discussed under each mask design in next section. Figure 4.3 shows the lithography mask that was used for the sensor fabrication. To optimize lithography mask, 4" wafer size was selected.

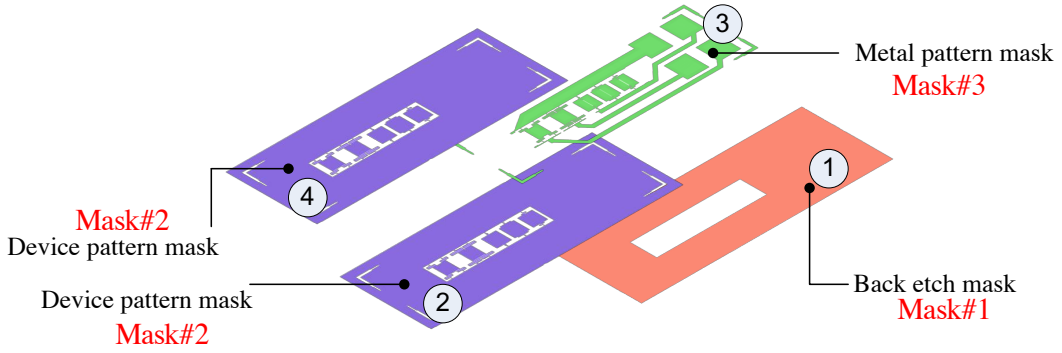

FIGURE 4.2: Lithography masks usage in different stages of fabrication. The fabrication step is followed by the circled number.

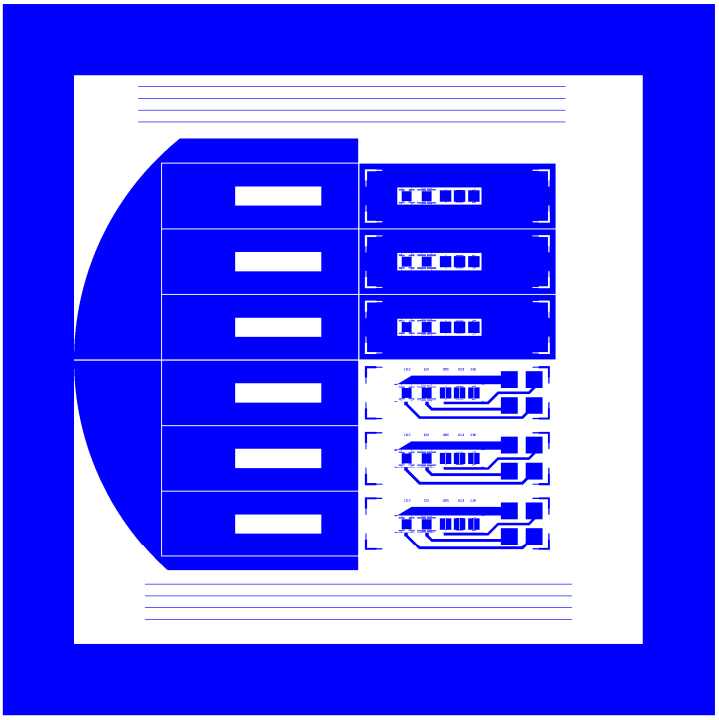

FIGURE 4.3: Picture of lithography mask design used for sensor fabrication.

4.1.2.1 Mask#1: Back etch hole pattern for KOH

Figure 4.4 shows the chip design with mirror platform for sensors and back hole cavity. The sensors are located in the mirror platform area. In a KOH solution, silicon with $< 100 >$ orientation etches in $< 111 >$ direction at a 54.74° angle. Considering this behaviour into account, assuming that only 10 μm is left after the KOH process, the width of the back hole mask (w_m) can be calculated using,

$$w_m = w_s + 2 \cdot h \cdot \cot(54.74°) \tag{4.1}$$

where w_s is the width of the mirror platform, and h is the the cavity height.

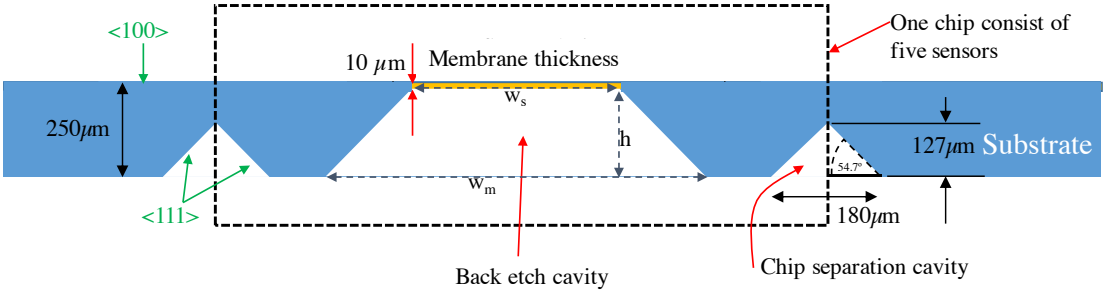

FIGURE 4.4: Chip design with back etch cavity.

4.1.2.2 Mask#2: Device pattern

This mask design is used to pattern the SiO_2 layer top of the Si. The SiO_2 layer acts as the insulator between Si and Al. In Figure 4.2, step#2 shows the mask#2 with SiO_2 pattern.

4.1.2.3 Mask#3: Metal pattern

This mask has patterns for separate bias voltage pads, conducting wires, and the sensor mirror. Figure 4.2, step#3 shows the mask#3 with Al pattern.

4.1.3 Protection for release etch

Before releasing sensors, mask#2 is used again for photoresist patterning to protect the Al and SiO_2 during the plasma Si etching process. Figure 4.2, step#4 shows the mask#2 with photoresist pattern.

4.2 Fabrication Process

The successful fabrication method is explained in this section. Sensors were fabricated in a class 100 clean room facility at the University of Manitoba. To fabricate the electric field sensors a 250 μm thick, n-type double side polished (DSP) Si wafer with $< 100 >$ orientation wafers was used. The wafer resistivity was 10-20 Ωcm (doping concentration 10^{16} - $2 \cdot 10^{16}$ cm^{-3}).

The fabrication process is involved following steps:

- Silicon wafers were cleaned with piranha for 15 minutes. H_2SO_4 to H_2O_2 ratio was maintained at 3:1. This removes any organic materials contaminating the silicon wafers.

- Both sides of the wafers were oxidized using the wet oxidation process. The silicon dioxide was grown to approximately 1.4 μm at 1100 °C. After cleaning, the photoresist was spun on both sides of the wafer and was patterned using the lithography process on back side. This is shown in Figure 4.2 .The thickness of the photoresist was 1.5 μm. BOE (Buffered Oxide Etching) was used on the exposed back side. Figure 4.5(a) illustrates this step in the fabrication process. Table 4.1 shows the wet oxidation recipe and Table 4.2 shows the backside patterning recipe.

TABLE 4.1: Wet oxidation recipe

Furnace temp	1100 °C
Heat(H_2O) temp	95 °C
N_2 flow rate	120 PSI

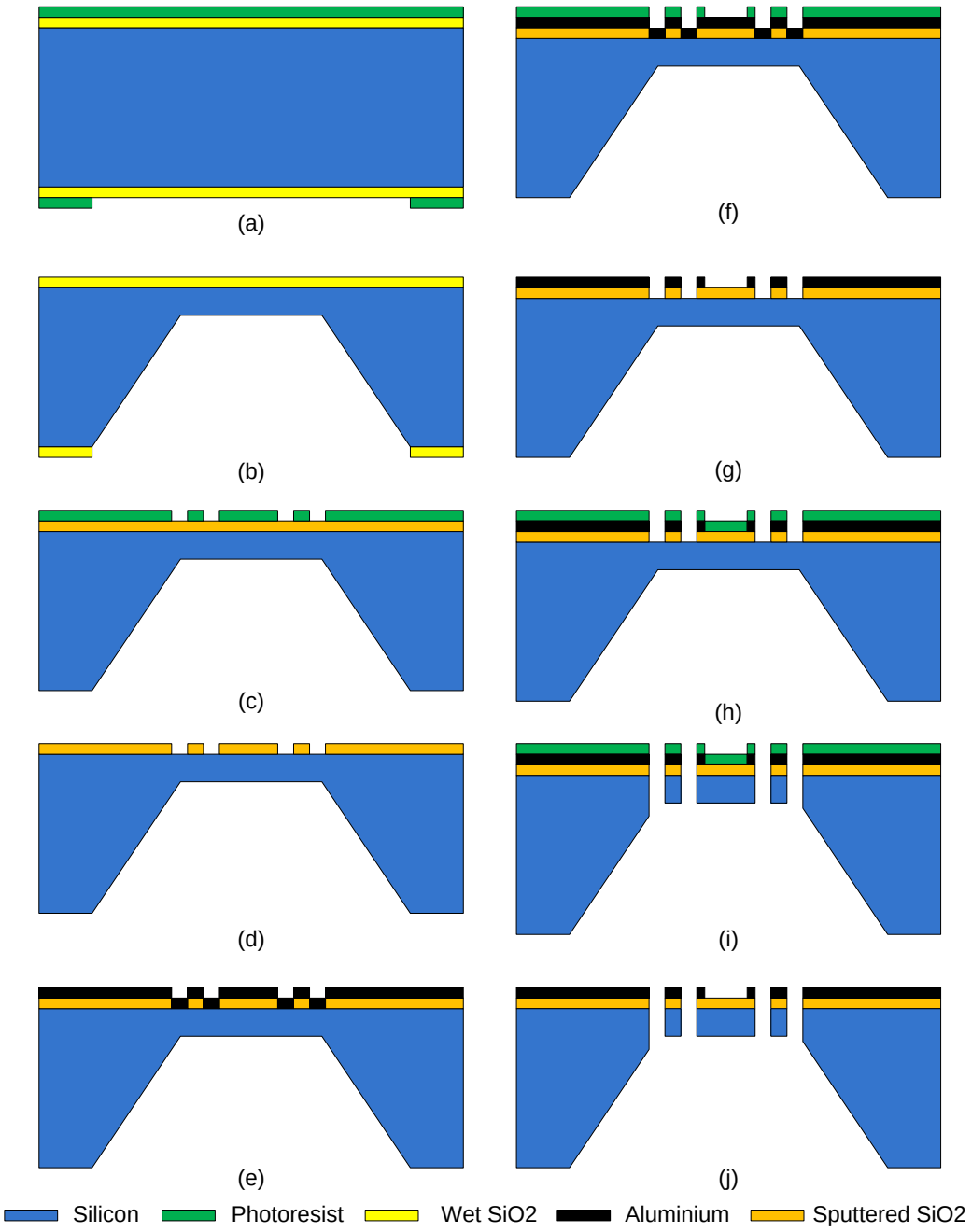

FIGURE 4.5: Complete fabrication process.

- Photoresist was removed using acetone, IPA, and water. Then the sample was etched using 30% KOH at 80 °C until 25 μm Si was left for the mirror platform. Figure 4.5(b) illustrates this step in the fabrication process. After

TABLE 4.2: Back side patterning recipe

Solution	HPR504
Humidity	51% 21.4 °C
Resist(rpm)/time(s)	500/5
Spread(rpm)/time(s)	500/10
Spin(rpm)/time(s)	3000/40
Soft bake/time(s)	110 °C/60
UV exposure(s)	3.5
Developing	40sec with MF354
Hard bake/time(s)	125 °C/90
Thickness	1.53 μm

that, samples were cleaned using piranha for 15 minutes.

- The SiO_2 layers were completely removed using the BOE process. Then, 50 nm of SiO_2 was sputtered on the top side of the sample. Thereafter 1.5 μm thick photoresist was spun and patterned. This step in the fabrication process is shown in Figure 4.5(c). The process parameters for sputtering the SiO_2 is shown in Table 4.3.

TABLE 4.3: SiO_2 Sputtering parameters

Parameter	Value
P_{base}	$7.1 \times 10^{-6}\ Torr$
P_{work}	$5.2 - 6.5 \times 10^{-3}\ Torr$
$Power_{RF}$	200/5 W
$Gas(Ar/O_2)$	30/15 $sccm$
$Time$	10 min
$Thickness$	50 nm

- The device pattern was extracted from the sputtered SiO_2 using BOE. Then the photoresist was removed using acetone, IPA and water. Figure 4.5(d) shows this step in the fabrication process.

- In this step, 500 nm of Al was evaporated on the top side of the sample at 17 Å/s. The base pressure during evaporation was 3.1×10^{-6} Torr. Figure 4.5(e) illustrates this step in the fabrication process.

- Photoresist was spun and patterned according to the *metal pattern mask*. Here, the step edge of SiO_2 was used as the alignment guideline during the lithography process. Figure 4.5(f) depicts this step in the fabrication process.

- The Al was patterned and etched using Al etchant to extract electrical mirror pads and electrical paths for the mirror. Etchant temperature was maintained at 70 °C and the liquid rotation speed was set at 300 *rpm*. Thereafter, photoresist was removed using acetone, IPA, and water. Finally, the samples were annealed in an N_2 ambient environment for 10 minutes. The annealing temperature was maintained at 350 °C and the N_2 flow rate was maintained at 130 sccm inside the oven. Figure 4.5(g) shows this step in the fabrication process.

- To protect Al and SiO_2 during the releasing step, photoresist was spun and patterned on the top side according to the device pattern mask. Figure 4.5(h) shows this step in the fabrication process. Table 4.4 shows the final device patterning recipe.

TABLE 4.4: Final device patterning recipes using lithography

Solution	HPR504
Dehydration bake/time (s)	115/90
Resist(rpm)/time(s)	500/5
Spread(rpm)/time(s)	500/10
Spin(rpm)/time(s)	3000/40
Soft bake/time(s)	110/60 then DI rinse
UV exposure(s)	3.5 s
Developing time	11 s with MF354
Hard bake/time(s)	125/90

- The device was released using a Trion plasma etch. First, to thin the device to 10 μm, approximately 10 μm were etched from back side of the sample. Then the sample was rotated up side down and a further 10 μm were etched

until all the designs were released. Figure 4.5(i) illustrates this step in the fabrication process. The Trion plasma Si etch recipe is shown in Table 4.5.

TABLE 4.5: Trion plasma Si etch recipe

Parameter	Value
Pressure	50 $mTorr$
ICP Power set	100 W
RIE Power set	50 W
SF6 set	30 $sccm$
Process Time	400 sec

- Finally, the photoresist was removed using a Trion plasma etcher. Figure 4.5(j) illustrates this step in the fabrication process. The Trion plasma device cleaning recipe is shown in Table 4.6.

TABLE 4.6: Trion plasma O_2 cleaning recipe

Parameter	Value
Pressure	100 $mTorr$
ICP Power set	100 W
RIE Power set	70 W
O_2 set	45 $sccm$
Process Time	200 sec

4.3 Fabricated Sensor Physical Measurements

The sensors were released with a Trion plasma etch. Thereafter, sensor dimensions such as thickness, spring width, over etch and under cut were measured with the Olympus BX51 microscope. Figure 4.6 shows the front side of the microscope images of all the fabricated sensors with their designed dimensions. At the end of this section designed sensor dimensions are compared with fabricated sensor.

For the most reflective results, the sensor surface (mirror side) should be very flat (horizontal) since an uneven mirror surface can disperse the reflected

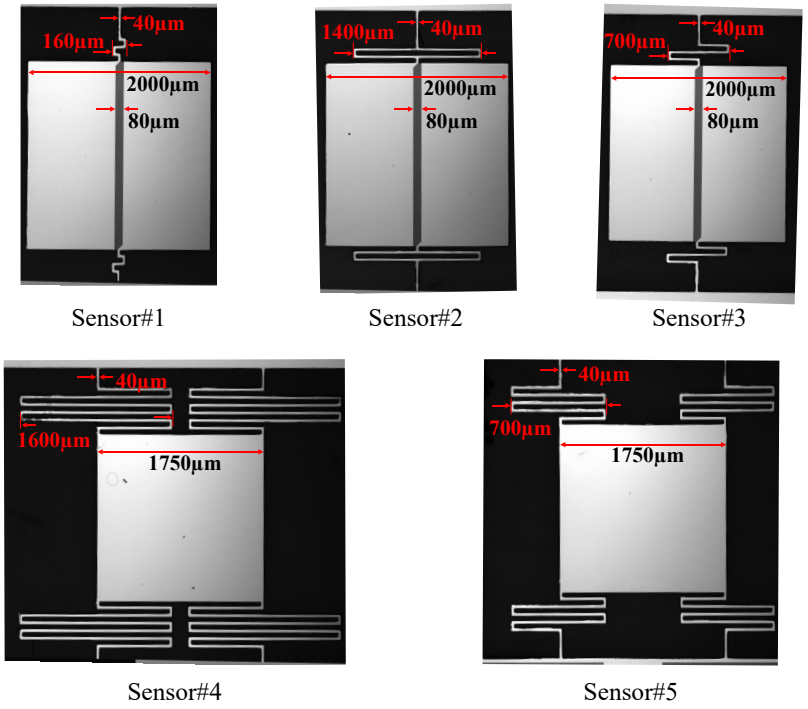

FIGURE 4.6: Microscope images of fabricated sensors. Sensor mirror platforms are designed as squares.

laser beam over the photodiode. Figure 4.7 shows front side sensor height measurements. Notice that, the sensors demonstrate a fine flat surface protecting a maximum height difference of less than 10 μm in all the designs due to reduced stress in the fabrication process. The lowest point on the surface is the center of each device, which is due to the uncompensated material stress.

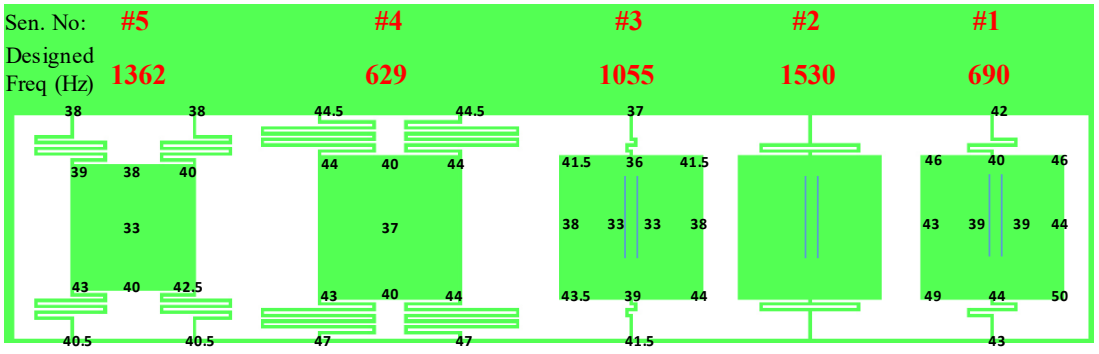

FIGURE 4.7: Sensor surface height measurements. Units are in μm.

Figure 4.8 shows the cross section of a fabricated torsional sensor. See that, sensor thickness is not even. After the backside etch (Figure 4.5(b)) the mirror platform thickness was 25 μm. But, after the release (Figure 4.5(i)), the back side of the sensor has uneven thickness and it is thickest at the centre. This is because the plasma release process etches the backside once it has complete the sensor release. Furthermore, notice that the sides of the mirror platform have over etched. This was due various etch rates in side the plasma chamber. The etch rate can vary due to a few parameters; such as sample orientation inside the chamber, effective etching area, and capability to remove by-products during the etching process. It can be concluded that during the release, the sides etched more than mirror platform center area. Figure 4.9 shows the microscope images of the back side of the released sensor and springs. This picture can be compared with Figure 4.8.

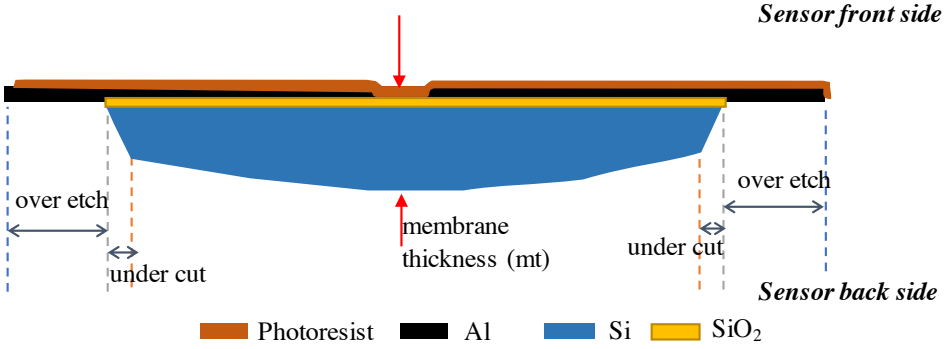

FIGURE 4.8: Torsional sensor cross sectional view after fabrication.

Table 4.7 shows comparison of the designed and fabricated sensor dimensions. It can be seen that springs have lower thickness and width compared to the designed sensor. As well as, the fabricated sensor, mirror platform average thickness is greater than the designed thickness. Parameters change resulted in the fabricated sensor to deviate from the simulated frequency.

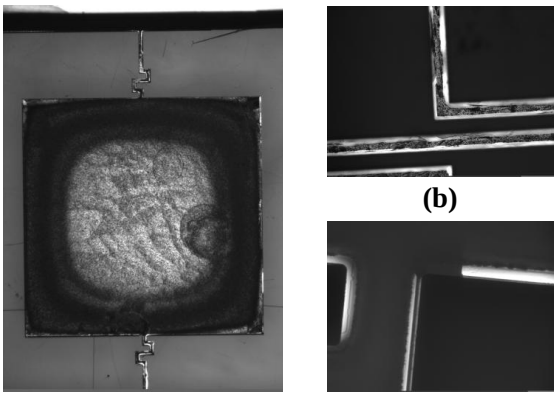

FIGURE 4.9: Microscope images of back side of fabricated sensor. (a) Back side of Sensor#3. Dark area has been etched more and center area has etched less. (b) Microscope is focused to the one of the sensors' top Si layer (according to the Figure). (c) Microscope is focused to the bottom (according to the Figure) of the sensor. Due to the over etch shiny Al layer is visible.

TABLE 4.7: Simulated and fabricated sensor dimensions comparison. (All dimensions are in μm.)

Sensor No	Designed	#5	#4	#3	#2	#1
Simulated resonance frequency (Hz)		1362	629	1055	1530	690
Fabricated sensor spring width (w)	40	20.5	22	18.8	-	20
Fabricated sensor spring thickness (st)	10	14	16	16	-	14
Fabricated sensor mirror platform average thickness (mt)	10	14.4	16	15.8	-	18

4.4 Development of flat sensor surface

In microfabrication, material stress is a common issue [22, 23]. During sensor fabrication, it was discovered that material stress was an issue and a solution is presented in this section.

4.4.1 Problem Identification

KOH back etch process was used to thin the sensor area up to approximately 25 μm during the fabrication. After the KOH process (Figure 4.5(b)), the membrane showed bending on the surface, as shown in Figure 4.10.

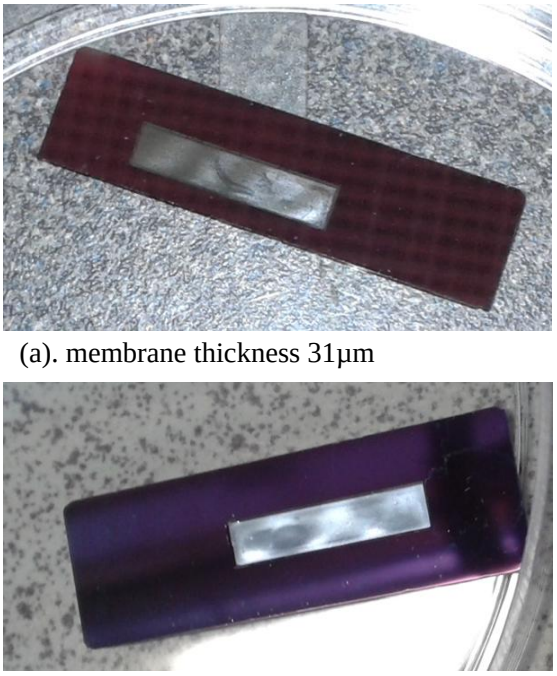

(a). membrane thickness 31µm

(b). membrane thickness 10 µm

FIGURE 4.10: Deformed mirror platform due to wet oxide compressive stress.

Due to different thermal expansion coefficients of the substrate and the thin films, compressive or tensile stress can cause deformations in the structure. The

wet oxidation is a high temperature process (1100 °C) and it leads to compressive stress of the deposited thin silicon dioxide film at room temperature. For more information about material stress please refer to Chapter 2 of Micromachined Thin-Film Sensors for SOI-CMOS Co-Integration [22]. The aim of the material stress relief experiments to compensate SiO_2 compressive stress by Al film tensile stress.

4.4.2 Procedure for Stress Measurements

In the sensor fabrication process only two thin films were used, SiO_2 and Al. Therefore, stress analysis was performed for the above two thin films using different deposition methods. For this task, single side polished (SSP), 3" wafers were used. For each method, three testing samples were used to increase accuracy of the results. The Toho FLX-2320 thin film stress measurement system was used for stress measurements (Figure 4.11) and measurements were taken at room temperature (∼22 °C).

FIGURE 4.11: Toho FLX-2320 thin film stress measurement system.

The Toho FLX-2320 thin film stress measurement system uses the principle of substrate curvature method for extracting the thin film stress. This gives an average stress of the thin film without knowledge of its Young's modulus and Poisson ratio [22].

4.4.3 Oxide Stress Analysis

SiO_2 stress analysis was performed using sputtering and wet oxidation methods. Sputtering was selected because it is a low temperature fabrication process that can be used for mostly substrates including those which can not withstand high temperatures [24]. Since this is a low temperature process less compressive stress can be expected.

As previously explained, wet oxidation is a high temperature process and causes higher compressive stress values. In this analysis, wet oxidation method is repeated to compare stress values with sputtering technique. those two techniques will be discussed in following sub-sections.

4.4.3.1 Sputtering of SiO_2

SiO_2 sputtering was preformed changing the applied power and Ar and O_2 air flow rates. The following steps were used to measure stress for three cases:

Step#1: Initial wafer thickness and stress was measured in cleaned bare samples.

Step#2: After sputtering, deposited film thickness, reflective index and stress were measured respectively.

Step#3: Three samples were placed inside the furnace and an hour of annealing

was performed at 1100 °C. N_2 flow rate was maintained at 130 sccm.

Step#4: Film thickness, reflective index, and stress was measured.

Step#5: Again, an hour of annealing was carried out for three samples at 1100 °C. N_2 flow rate was maintained at 130 sccm.

Step#6: Film thickness, reflective index, and stress was measured.

Figure 4.12 shows sputtered SiO_2 stress measurements during different stages of the process. Sample names are SPox1, SPox2 and SPox3. This Figure shows that SiO_2 has lower compressive stress just after sputtering. However, annealing increases the compressive stress. Table 4.8 shows the fabrication parameters used for the three samples.

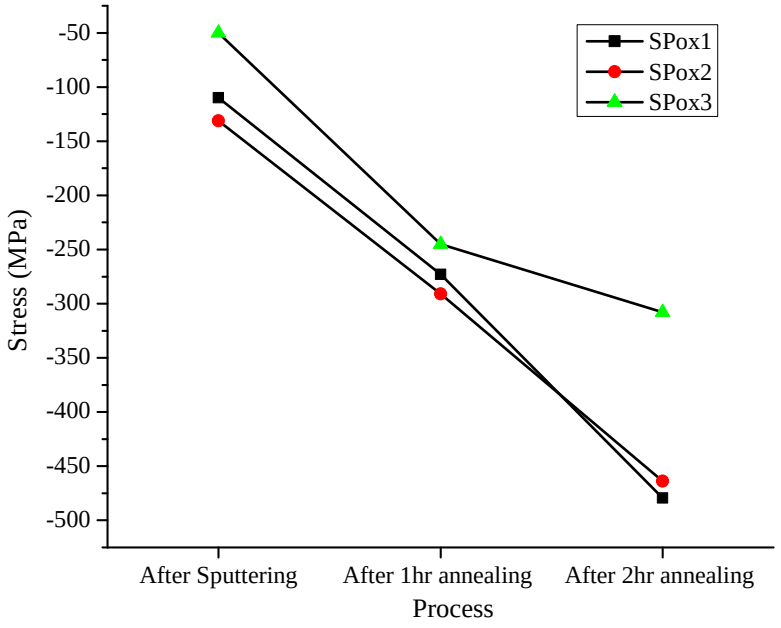

FIGURE 4.12: Sputtered oxide stress variation after each step.

TABLE 4.8: SiO_2 sputtering recipes for stress analysis.

Sample No	**SPox1**	**SPox2**	**SPox3**
Base Pressure ($\times 10^{-6}$ Torr)	4.3	4.3	4.3
Working Pressure (mTorr)	5.4-6.6	5.4-6.6	6.1
RF Power (W)	200/5R	300/5R	300/5R
Ar Flow (sccm)	30	30	15
O_2 Flow (sccm)	15	15	30
Depo. Time (sec)	600	600	600
Thickness (nm)	48.5	89.2	79.1
Growth Rate (nm/sec)	0.08	0.149	0.132
T1	88	88	88
Film Stress (Mpa)	-109.9	-131.17	-50.07
Tensile/Compressive	C	C	C
Remarks	11 K	11 K	11 K
Reflective index (at 632.8 nm)	1.471	1.472	1.47

4.4.3.2 Wet Oxidation of SiO_2

It is known that wet oxidation causes high compressive stress due to higher temperatures used in the technique. This test was performed to identify stress values in different wet oxide film thicknesses. The samples were labelled as wet_ox1, wet_ox2, and wet_ox3 . The procedure for this experiment is as follows.

Step#1: Initial wafer thickness and stress was measured.

Step#2: Furnace was heated to 1100 °C and oxidation done for ∼5 hours to grow 1.1 μm of oxide. N_2 flow rate inside the furnace was maintained at 120 sccm and water temperature was set to 90 °C.

Step#3: After samples were cooled to room temperature, oxide thickness and stress measurements were taken. During the wet oxidation, both sides of the wafer the samples were covered with SiO_2.

Step#4: Back side (not polished side) SiO_2 was removed completely and stress was measured on the front side.

Step#5: SiO_2 thickness was reduced by etching in BOE to around 550 nm and

stress was measured.

Step#6: Again, SiO_2 thickness was reduced by etching in BOE to around 300 nm and stress was measured.

Figure 4.13 shows the stress measurement after each step. It can be seen that when both sides of the wafer are covered by an oxide film, stress is lower because compressive stress is cancelled out each other due to it is in opposite sides. But, when the oxide is only in one side it has a high compressive stress. When reducing the oxide thickness, it can be seen that comressive is increasing as a function of oxide thickness. Lowest compressive stress can observe when the oxide at one side of 270 MPa.

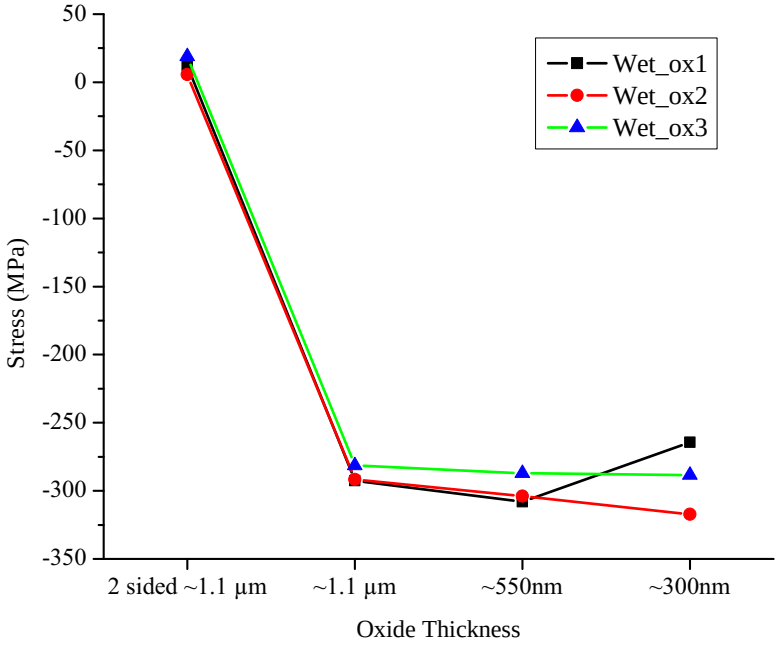

FIGURE 4.13: Wet oxide (SiO_2) stress variation with the thickness.

4.4.4 *Al* Stress Analysis

There are a few aluminium deposition techniques available at nano-fabrication laboratory, which are *Al* sputtering and *Al* evaporation. Only *Al* evaporation

deposition is considered for stress analysis.

For a smooth and shiny surface *Al* evaporation is preferred at a higher evaporation rate.

Aluminium evaporation was carried out for three 3" SSP wafers. The samples were named Al1, Al2, and Al3; and where the *Al* layers were of thickness 300 nm, 500 nm, and 800 nm thin respectively. Different thicknesses of the thin films should lead to different tensile stress values. Test procedure is listed as follows.

Step#1: The substrate thickness and initial stress was measured.

Step#2: *Al* was evaporated to 300 nm, 500 nm, and 800 nm using the evaporating system.

Step#3: Deposited film thickness and stress was measured (just after evaporation).

Step#4: Three samples were annealed for 10 minutes in the a furnace at 350 °C and N_2 flow rate was maintained at 120 PSI.

Step#5: *Al* film thickness and stress was measured at room temperature.

Step#6: Again, Step#4 was repeated.

Step#7: Again, Step#5 was repeated.

Step#8: Again, Step#4 was repeated.

Step#9: Again, Step#5 was repeated.

Figure 4.14 shows stress values after each measurement. Notice that annealing causes to higher tensile stress. Just after evaporation of *Al* showed a compressive stress. However, with annealing compressive stress turned to a tensile stress and rapidly increasing until 20 minutes.

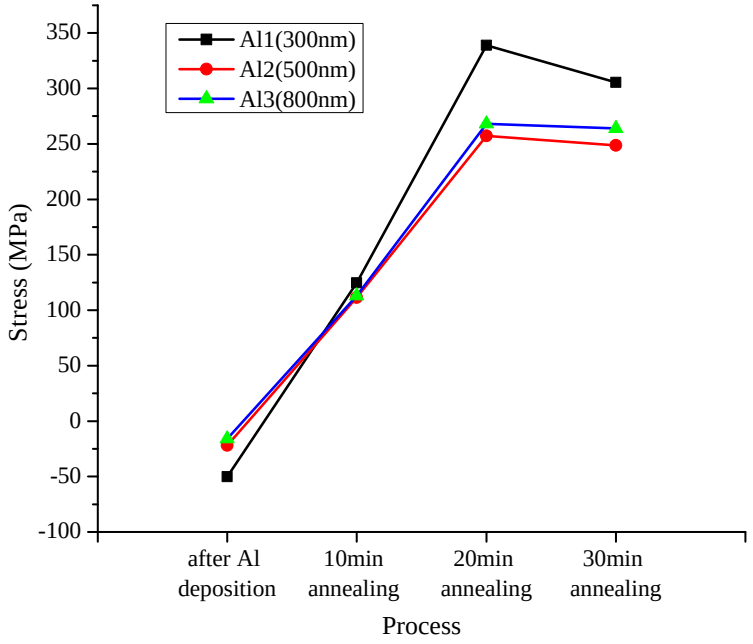

FIGURE 4.14: *Al* stress measurements in different steps.

4.4.5 Conclusion

From the above tests, it can be seen that different process conditions change the compressive and tensile stress magnitudes of SiO_2 and Al respectively. We can conclude that it is possible to reduce stress in the whole device by using the correct deposition techniques for SiO_2 and Al. Where the compressive stress is cancelled out by the tensile stress.

Figure 4.12 shows the SPox1 sample had 110 MPa of compressive stress just after sputtering. Also, in Figure 4.14, Al2 sample had 111 MPa of tensile stress after 10 minute annealing. This combination was used for the device fabrication. It was shown that sputtered SiO_2 (sample SPox1) for has very good reflective index (1.47), close to Fused silica (1.457).

4.5 Fabrication trials

This section mainly focus on problems related to fabrication and corresponding solutions. Several trials with different parameters were performed to identify successful device fabrication process. Processes were tuned by testing on dummy samples and then, applied on real samples.

4.5.1 Plasma etching for device release

Plasma etch was a very important process during the device fabrication. A Trion RIE/ICP plasma etcher was used in this step. Several dummy samples were used to calculate Si, SiO_2, and photo resist etch rates and impact on photoresist during the device release.

4.5.1.1 Photoresist strength test

For the final releasing step (Figure 4.5(i)), photoresist was used as a protective layer top side of the sensors. Therefore, the survivability of a 1.4 μm thick photoresist was tested in a dummy wafer. It was required to left some photoresist after this test.

Table 4.9 shows the etching parameters of the test. After, 1000 s etch time, the remaining photoresist thickness was 700 nm. Therefore, 1.4 μm thick photoresist is enough during the final releasing step.

TABLE 4.9: Photoresist strength test recipe.

Pressure	50 mTorr
ICP Power set	100 W
RIE Power set	50 W
SF_6 set	30 sccm
Process Time	1000 sec

4.5.1.2 Photoresist removal from the released device

As previously explained, photoresist was used as a protective layer during device release. However, for better reflective results of the mirror platform, photoresist was needed to be removed after the device release. Figure 4.15 shows released device with photo resist on the sensor surface.

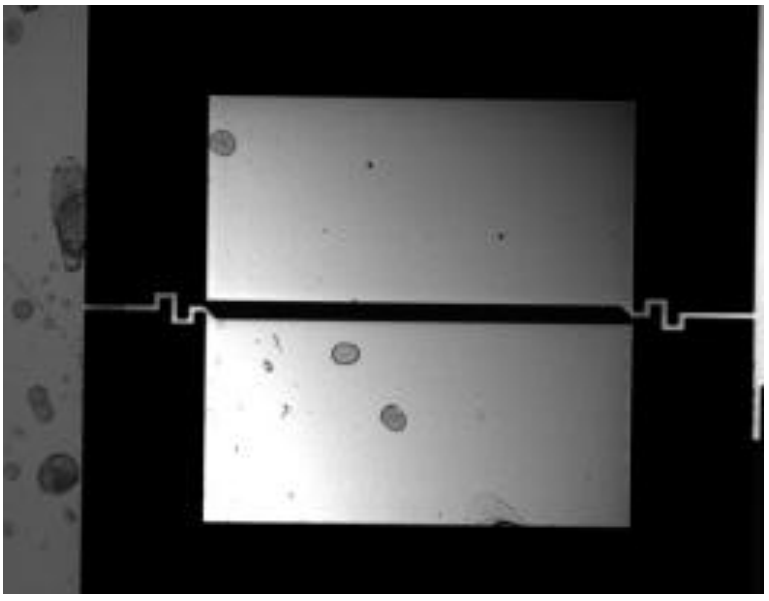

FIGURE 4.15: Released sensor with photoresit on it.

Attempt 1: Solvent to remove photoresist

In this attempt, the photoresist was cleaned with Acetone and IPA. acetone has higher evaporation rate than IPA. Therefore, to avoid risk of breaking the

sample, the device was submerged in acetone for 10 min and quickly transferred to a IPA solution and kept there for 2 minutes. Then, sample was air dried.

Observations – Figure 4.16 shows, photoresist was not completely removed and created new problems. Folded springs are disoriented in Figure 4.16 (a) due to undissolved photoresist. Figure 4.16 (b) shows mirror platform with a cloudy surface.

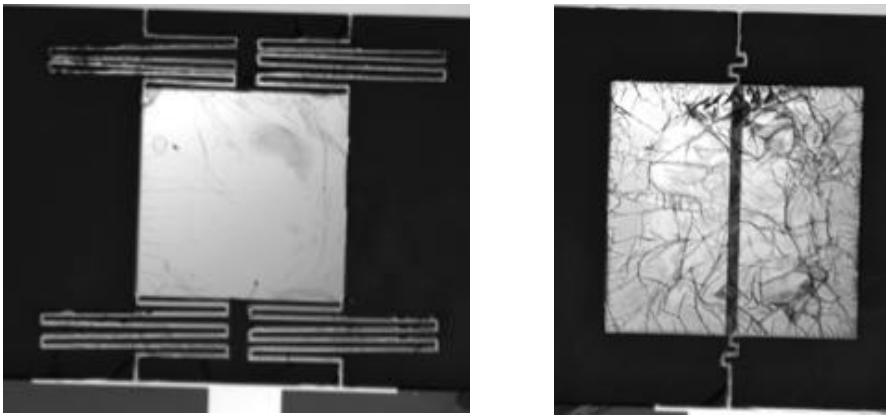

FIGURE 4.16: Microscope images of sample after cleaning with Acetone and IPA. (a) Some folded springs has disorientated. (b) Membrane area has become cloudy. Not good for reflecting.

Attempt 2: Plasma clean of photoresist

In this attempt, the Trion plasma was used with O_2. Here, O_2 reacts with photoresist and will be removed from the surface. Trion plasma recipe is shown in Table 4.10.

TABLE 4.10: O_2 Trion plasma cleaning recipe.

Pressure	$100mTorr$
ICP Power set	$100W$
RIE Power set	$70W$
O_2 set	$45sccm$
Process Time	200sec

Observations – Figure 4.17 shows a microscope image of a sensor after O_2 clean. Photoresist was completely removed. However, some residual Si is visible. This can be removed by back side Trion plasma Si etch.

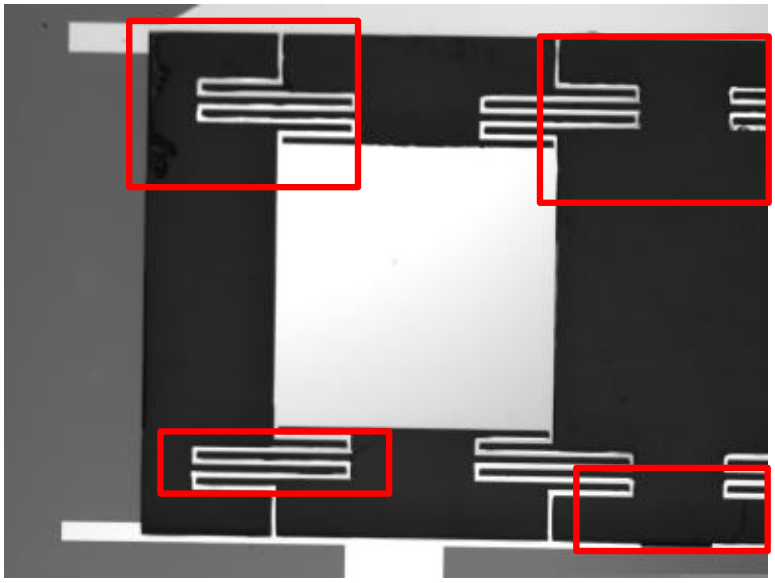

FIGURE 4.17: Microscope image of a sensor with not released Si residues.

Chapter 5

Testing and Results

This chapter describes how the test set-up was designed, presents test results and frequency comparison between simulated and fabricated sensors.

5.1 Lab bench test set-up overview

This section explains the tasks of different components used in the test set-up. Figure 5.1 shows the overview of the set-up.

The sensor biasing circuit generates two opposite sinusoidal voltages (V_{ac1} and V_{ac2}) for the sensor electrodes and the reference signal for the lock-in amplifier. The laser interrogated sensor circuit measures the sensor motion using a photo detector. The photo detector outputs a proportional current quantity according to the sensor motion and it is sent to the signal processing circuit. The signal processing circuit consists of the I to V (current to voltage) converter, lock-in amplifier, phase inverter, digital multimeter and PC for data acquisition.

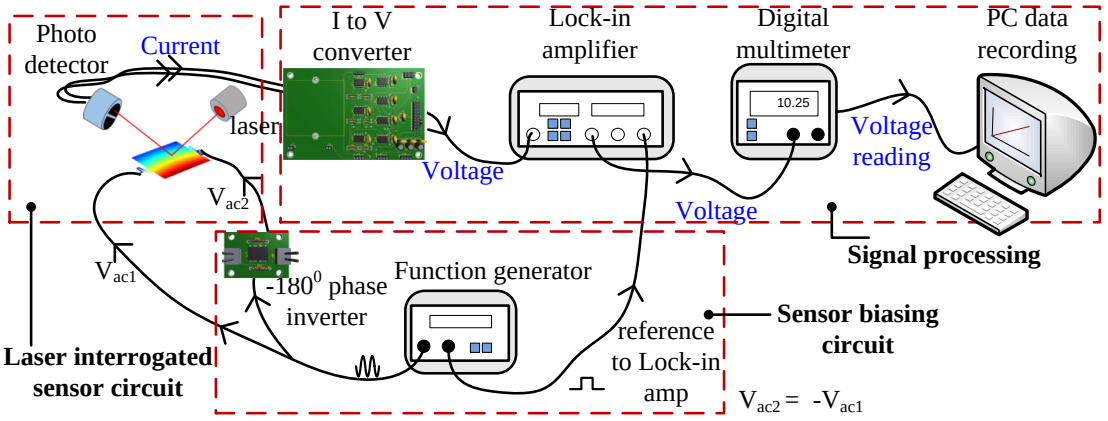

FIGURE 5.1: Overview of test set-up.

5.1.1 Laser interrogated sensor circuit

Figure 5.2 shows the acrylic frame design for the laser interrogated sensor circuit. Because of the triangle shape, laser alignment (bouncing and detecting) is easier than other shapes.

- The sensor is mounted on an *Al* metal ring (Figure 5.2 right). This metal ring is earth grounded to avoid building up of any floating potentials. These floating potentials can change the sensor reading significantly as these can create a higher electric fields with the close proximity sensor.

- The differential photo detector (SD113-24-21-021) has two splits (PD_A and PD_B), and it is aligned with the sensor such that it would detect the main beam from the laser diode.

- The calibration plate below the sensor is used for sensor calibration purposes. Distance between the sensor and the calibration voltage plate is 1.5 cm. When a known dc voltage is applied to the calibration plate the sensor response can be measured from the digital multimeter.

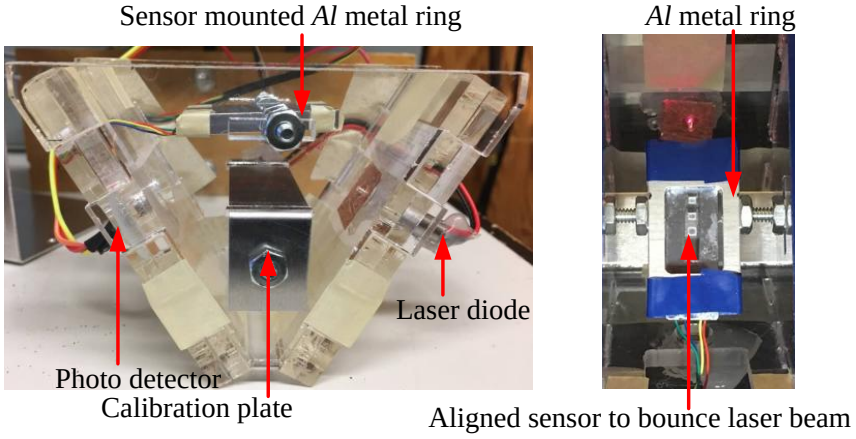

FIGURE 5.2: Acrylic frame consist of sensor, laser, photo detector and calibration plate.

5.1.2 Sensor biasing circuit

Sensor biasing circuit consists of a signal generator and a phase inverter.

5.1.2.1 Signal generator

The signal generator (GwIBNSTEK AFG-2005) creates the ac bias for the sensor and the sync reference for the lock-in amplifier. The ac signal is divided into two paths such that one is fed to a phase inverter and the other to the directly to the sensor.

5.1.2.2 Phase inverter

Figure 5.3 shows the phase inverter schematic. The phase inverter consists of OP27 [25] low noise op-amp in an inverting configuration with a gain of one. This gives a phase shift of 180 degrees creating an opposite polarity voltage to the sensor electrode 2 (V_{ac2}). The delay in the inverter circuit is negligible with the sensor operating frequency.

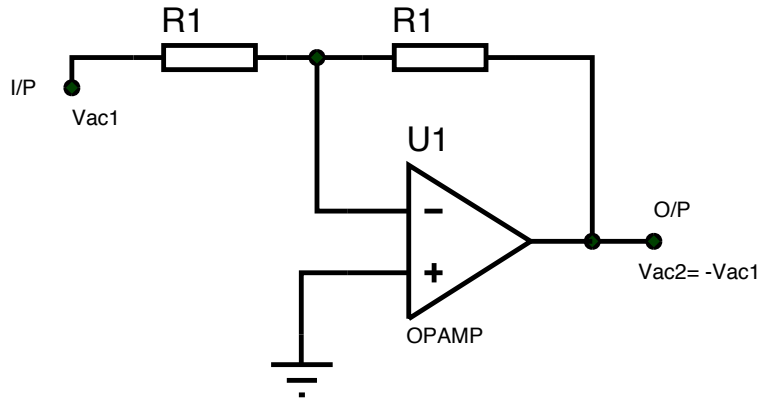

FIGURE 5.3: Phase inverter schematic.

5.1.3 Signal processing circuit

5.1.3.1 Lock-in amplifier

The lock-in amplifier (SRS510) acts as a band pass filter that can be tuned to a specific frequency. It filters the desired frequency component from a noisy signal.

5.1.3.2 I to V (current to voltage) converter

Figure 5.4 shows the block diagram of I to V converter and the summing function. The outputs of the differential photo-detector (PD_A and PD_B) are fed to I to V converter circuits. This circuit has a bandwidth of 1.6 kHz and gain of 10^4. The summing circuit acts as a differential amplifier circuit. It has a bandwidth of 16 kHz and gain of 10. For information about this circuit refer [12] pages 50-57.

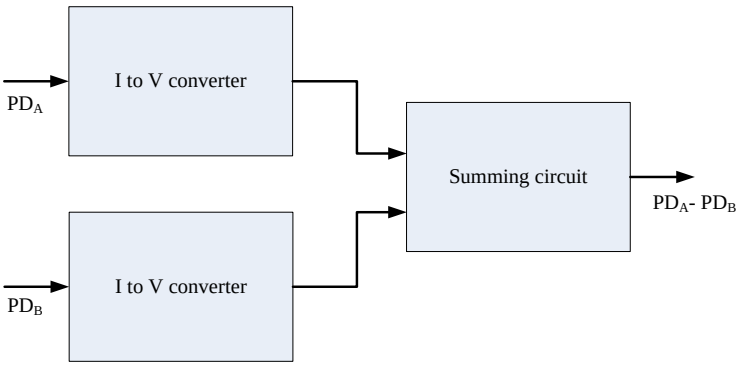

FIGURE 5.4: I to V converter block diagram.

5.1.4 Digital multimeter and PC

The lock-in amplifier output is measured by digital multimeter (Agilent 34461A) and the measurements are recorded in a PC.

5.2 Lab Bench Testing

5.2.1 Faraday Cage

Figure 5.5 shows the sensor mounted laser interrogated system placed in a Faraday cage. The Faraday cage is made from aluminium (Al) and earth grounded. This structure ensures that external electric fields will not affect the sensor measurements. In Figure 5.5, the lid of the Faraday cage is open for the purpose of showing an inside view.

5.2.2 Testing procedure

The sensor mounted acrylic frame was placed in the Faraday cage with connecting electronics and the cage was closed. Then a known voltage was applied to the

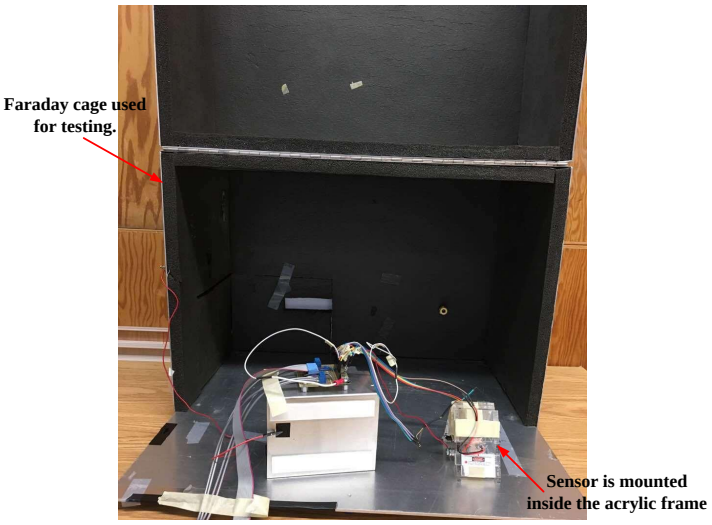

FIGURE 5.5: Acrylic frame with sensor inside the Faraday cage. Black box is the Faraday cage.

calibration plate. Sensor responses were recorded in the PC. It was assumed that for different voltages the fringing effect is minimum from the calibration plate.

Figure 5.6 repeats Figure 4.7 to remind sensor numbering. The sensor#2 was not tested because of one spring was broken during the releasing step. The response from Sensor#4 and #5 were small due to increased spring stiffness and the increased membrane thickness (mass) during the fabrication. Therefore, testing of sensor numbers 2, 4 and 5 will not be discussed in this thesis.

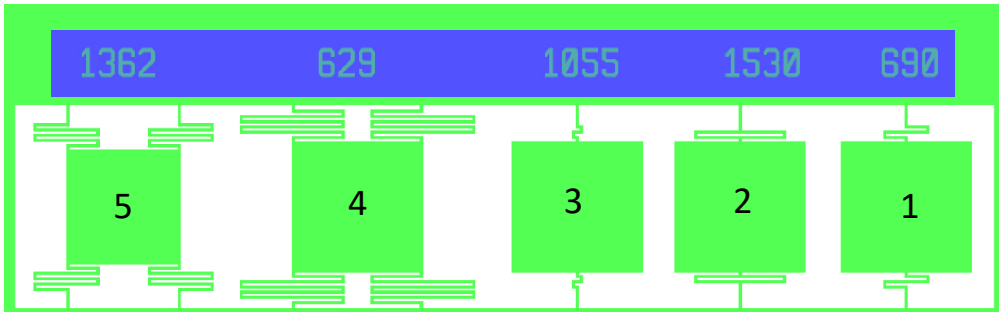

FIGURE 5.6: Sensors with numbers.

5.2.3 Resonance frequency of fabricated sensors

The mechanical resonance frequency of sensors were investigated after releasing the devices. The resonance frequency gives the relative maximum response for the sensor motion.

A frequency sweep was performed from 100 Hz to 1500 Hz to find the resonance frequency of each sensor. Figure 5.7 shows the sensor output (V_{rms}) obtained from the frequency sweep for sensor#1 (690 Hz) and sensor#3 (1055 Hz) under a 8 kV/m electric field and a 14.2 V_{pp} sensor bias voltage .

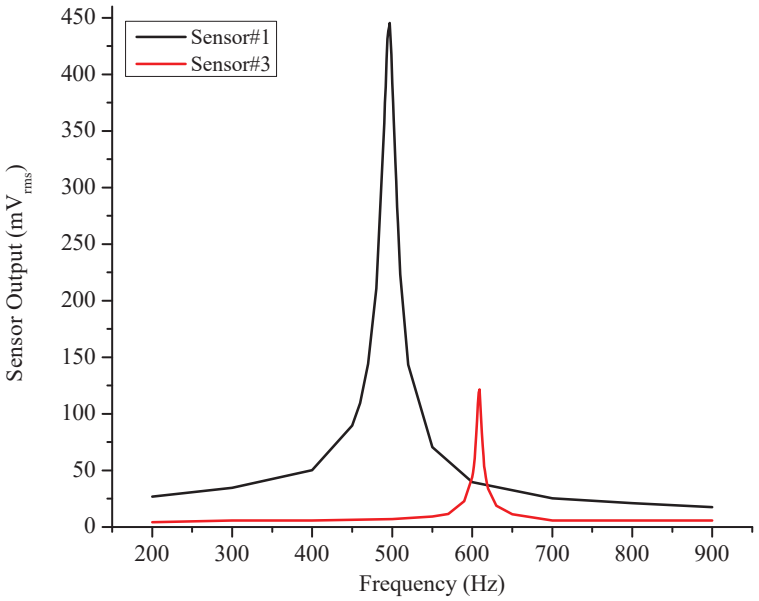

FIGURE 5.7: Frequency sweep of the sensors.

According to Figure 5.7, sensor#1 (690 Hz) has a maximum response of 445 mV_{rms} at 497 Hz and the sensor#3 (1055 Hz) has a maximum response of 121 mV_{rms} at 609 Hz. Different responses for the two sensors at resonance mainly depend on the spring stiffness of the sensors as discussed in Chapter 3.

Table 5.1 compares the designed and fabricated sensor frequencies. It can be noted that the measured sensor resonance frequency is lower than the design

frequency. This is due to fabricated sensor dimensions are not exactly matched with design parameters (Table 4.7).

TABLE 5.1: Simulated and fabricated sensor frequency comparison.

Sensor No	#5	#4	#3	#2	#1
Designed resonance frequency (Hz)	1362	629	1055	1530	690
Measured resonance frequency (Hz)	-	-	609	-	497

5.2.4 Lab bench testing results

Figure 5.8 shows responses for different calibration plate voltages and bias voltages for sensor#1 and sensor#3.

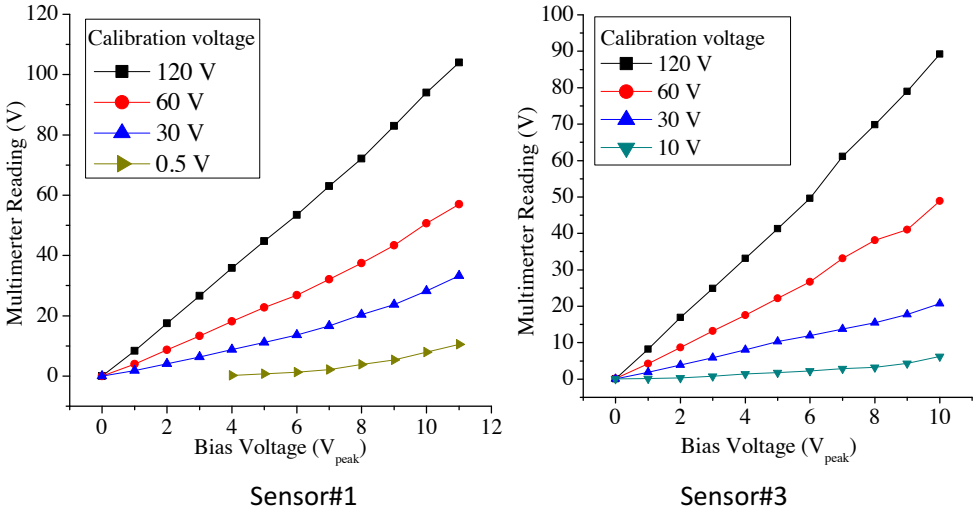

FIGURE 5.8: Lab bench test results for different calibration and bias voltages.

It can be seen that both sensor responses increase when measuring higher voltages (A calibration voltage of 120 V creates around 8 kV/m electric field). But, at lower electric fields, sensor response is not linear. This non-linearity is because the sensor is measuring other fields in the environment such as interference from near by sensors and the voltage paths. When measuring of an electric field, that is

more significant than the electric fields created by other sources, sensor response becomes linear.

5.3 Portable enclosure box and electronics

5.3.1 Introduction

It was required to develop a portable system to remotely measure the electric field under dc power lines for Manitoba Hydro. Laboratory instruments are difficult to handle in test site conditions and therefore functions of lock-in amplifier, signal generator and data logging were integrated into this system. Figure 5.9 shows the complete electric field measuring system that was developed for outdoor testing.

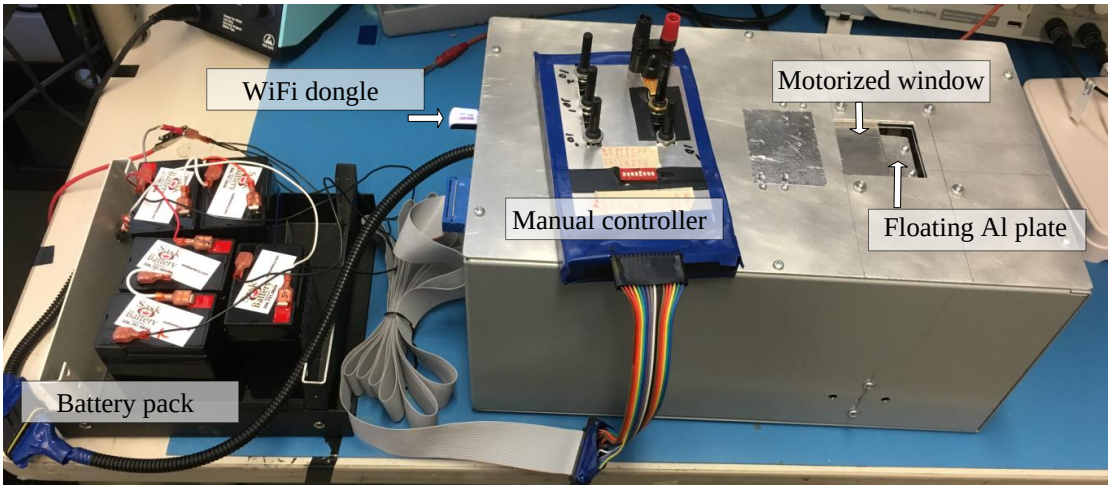

FIGURE 5.9: Portable electric field measuring system developed for outdoor testing.

5.3.2 Enclosure box design

Figure 5.10 shows the cross section of the enclosure box design. It consists of two *Al* boxes. The inner *Al* box protects the sensor. The outer *Al* box protects

electronics, and and gives the option of isolating the sensor in order to remove space charges that collects on the floating *Al* metal plate.

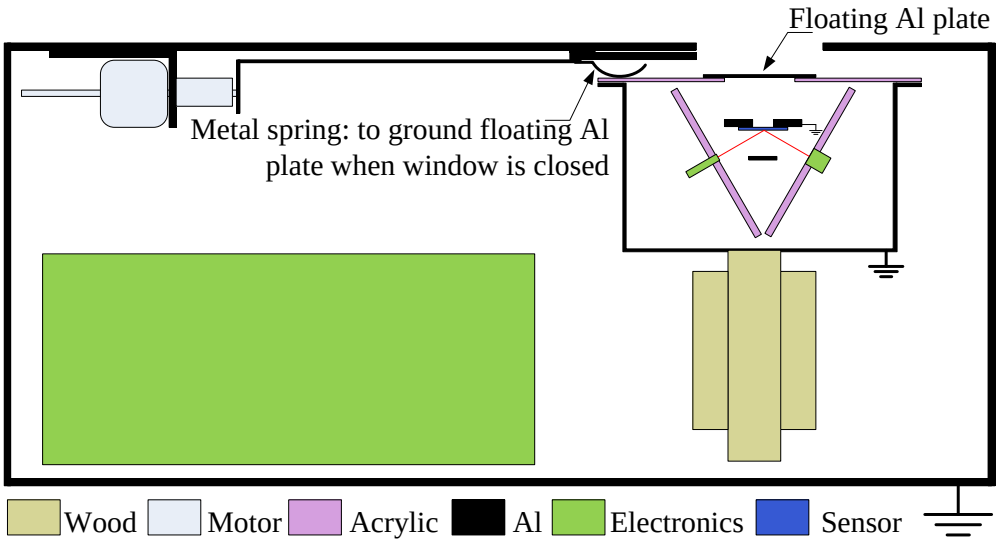

FIGURE 5.10: Cross section of the portable enclosure box.

The outer *Al* box has a window that is controlled by a stepper motor. The motor shaft can be moved back and forth to open and close the window. The inner box has an acrylic lid with a hole which is covered by an electrically floating *Al* metal plate same size as the window (Figure 5.11 right). When the window is opened this *Al* metal plate is exposed to outside electric field. When the window is closed, the floating *Al* metal plate is grounded through a metal spring connected to the window (Figure 5.9). The inner box is fixed to the outer *Al* box using the wooden blocks.

When the window is opened, an external electric field can passes through the opening and reach the sensor. The sensor mounted on the *Al* base inside the inner box and this *Al* base is grounded. Therefore, most of electric flux is engaged in sensor area.

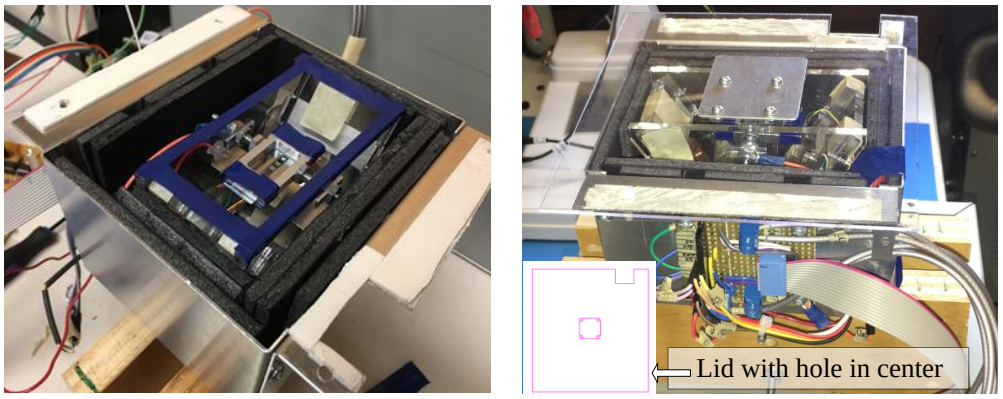

FIGURE 5.11: Inner *Al* box configuration.; Left: Sensors are mounted on the *Al* base connected to acrylic frame. Right: Inner box structure with electronics wiring. Floating *Al* plate has mounted to the acrylic lid over the hole.

5.3.3 COMSOL simulations of enclosure box

Simulations for electric field distribution were done in COMSOL multi-physics software considering actual physical parameters of the enclosure box design. These results were used to fine tune the box configuration up-to the final working prototype to measure the external electric field. Optimum size of the window size, distance to the sensor from window are suggested as future work.

Figure 5.12 shows the cross section of the designed box with electric field distribution for a 2 kV/m electric field. ($V_s = 1$ kV source voltage is applied at 50 cm distance from the outer box.) Just after the electric field passes through the window, the electric field starts to drop significantly. Due to sharp edges of the box higher electric field is created (fringing fields), but it is not affecting the top of the floating *Al* plate. Everywhere on the outer box except the window area has a uniform 2 kV/m electric field.

Figure 5.13 shows electric field drop down with different sizes of floating *Al* plates and plots are shown for a vertical center line through the window. For the case of 2.7 cm lid size can be compared with Figure 5.12.

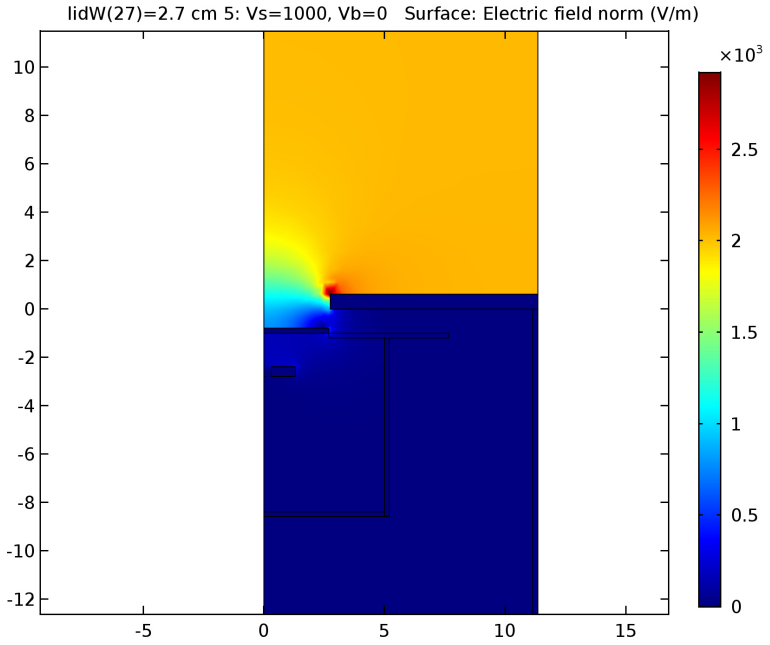

FIGURE 5.12: COMSOL simulation of enclosure box.

Figure 5.13 shows for the case of $V_s = 1$ kV , $lidW = 2.7$ cm and $V_b = 0$ V, the electric field is reduced at the sensor location by 11 times. Where V_s is the source voltage, $lidW$ is the width of the lid, and V_b is the sensor bias voltage.

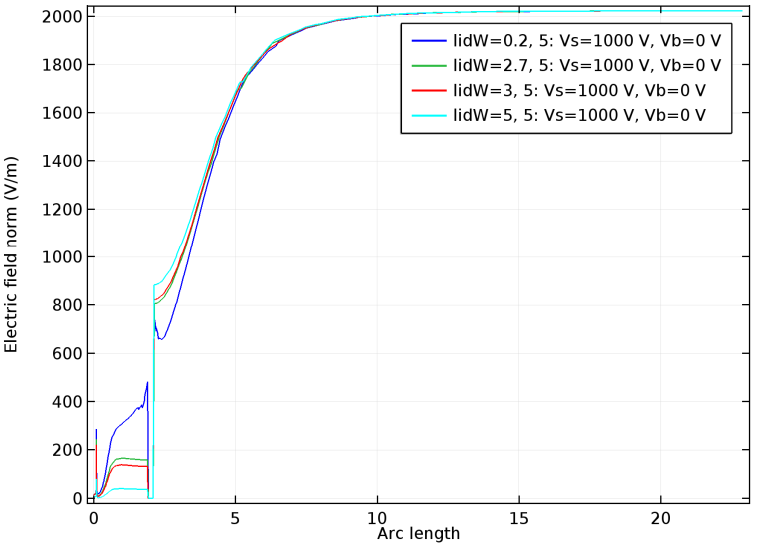

FIGURE 5.13: Electric field drop for different floating lid sizes.

It can be seen that the electric field strength has dropped significantly when

it passes through the window in the box. The reach of the electric field to the sensor depends on few parameters. window size, floating *Al* plate size, distance to the sensor from the window and distance to the nearest ground from the window.

5.3.4 Portable electronics system design

Figure 5.14 shows the functional block diagram of the portable electronic system. The portable electronic system replaced instruments were used in the lab-bench test set-up. The function generator was replaced by the low power, programmable waveform generator AD9833, the lock-in amplifier was replaced by the high precision balanced modulator/demodulator AD630. The digital multimeter was replaced by the 10-bit, analog to digital converter (ADC) MCP3008. The PC was replaced by a Raspberry Pi2 (RPI) single board computer (SBC) which performed the data logging and the system control functionalities.

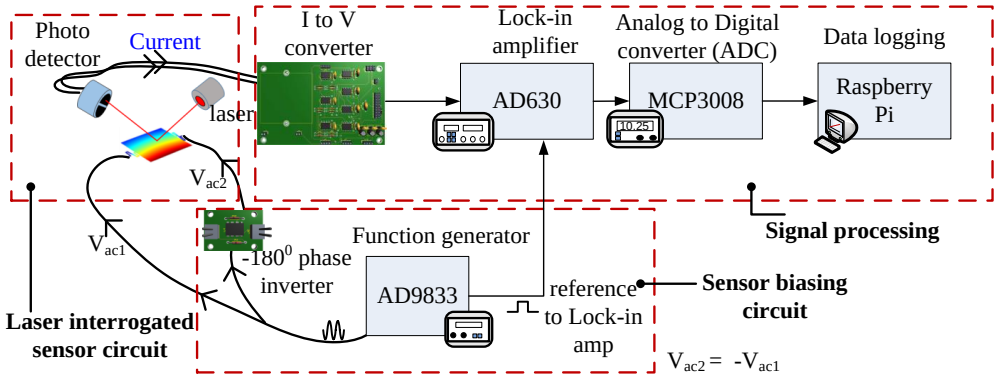

FIGURE 5.14: Functional block diagram.

The developed electronics system can change sensor frequency, sensor bias voltage and data sampling speed. It is also capable of recording data in real-time and take instantaneous measurements from a remote location through a local WiFi network . The RPI is used as the main processor for semi automated system to run the overall system software, record data, setup a local WIFI network to send

data to a laptop. An Arduino Mega micro controller is used to control relays, motor driver and manual operation of the system. Figure 5.15 shows the overview of the complete system and Figure 5.16 shows the developed electronic circuits for the portable system.

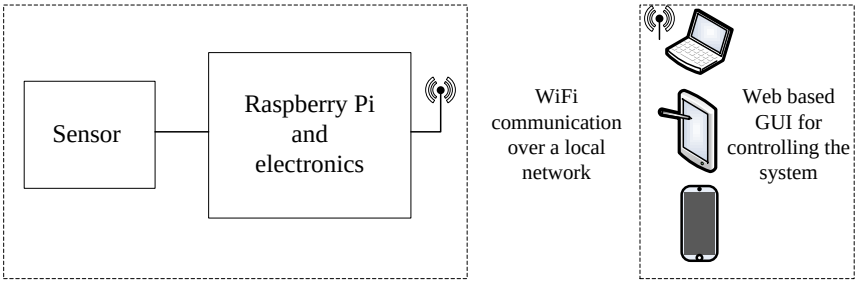

FIGURE 5.15: Portable system overview.

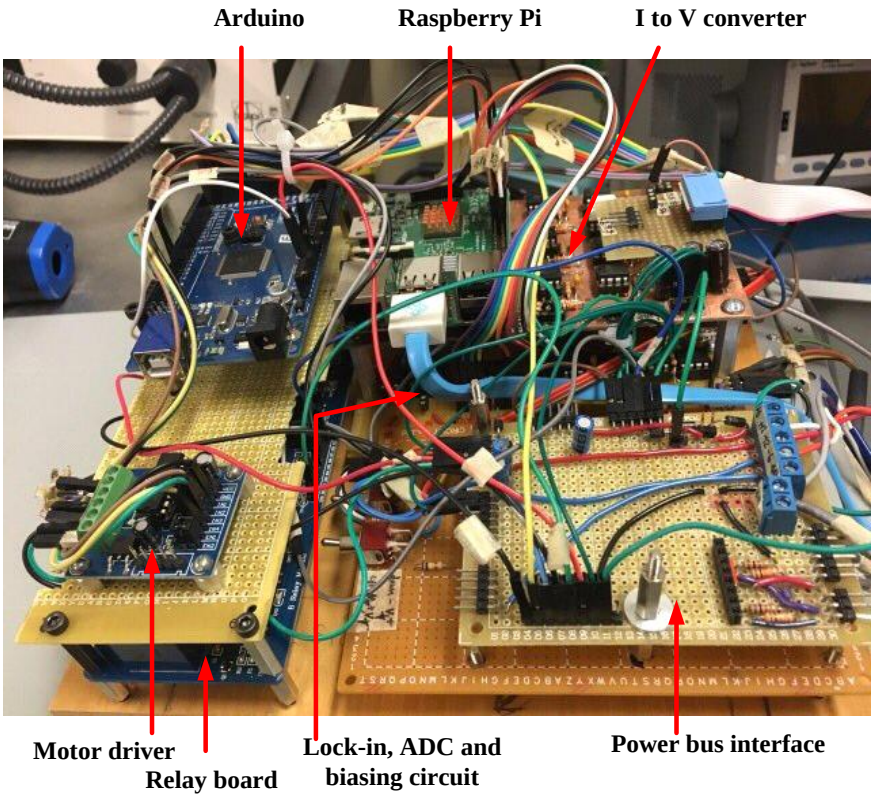

FIGURE 5.16: Sensor electronics.

The RPI runs in a Linux operating system and it was selected to reduce the development time, availability of sufficient general purpose input and outputs

(GPIO), and simplicity with integrating low level hardware peripherals. The RPI was programmed using the Python language. Serial peripheral interface (SPI) was used to communicate with ADC [26], sine wave generator [27], and bias voltage gain controller [28].

The sensor electronics was powered by 12 V Lead-Acid battery packs and system power consumption was about few watts (∼5 W). WiFi enabled devices, such as a laptop, a tab or a mobile phone can be connected to the RPIs' local WIFI network to control settings and record data using the web based graphical user interface (GUI). Integrating a micro-controller based system, power consumption can be reduced to milliwatts range and this is suggested as future work.

5.3.5 Web based graphical user interface (GUI)

The GUI was developed using the PHP and HTML languages, and the sensor data can be saved to a MySql database. Figure 5.17 shows the screen-shot of the designed GUI for the portable system.

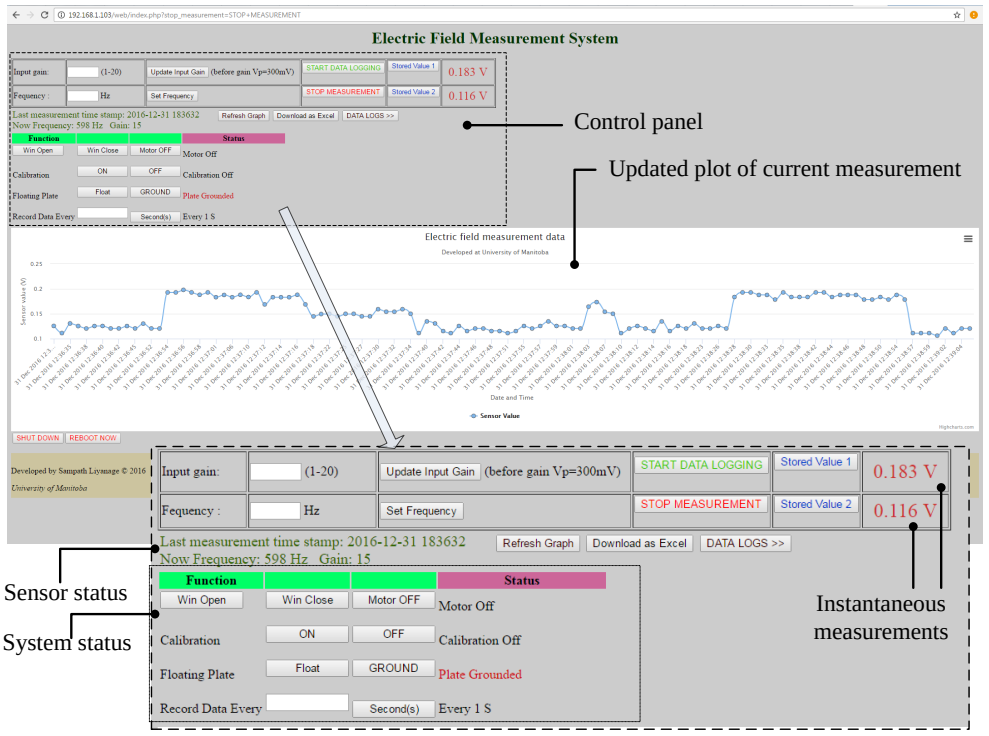

FIGURE 5.17: Web based GUI for controlling the system.

5.4 Electric field measurements with developed electronics system

The sensor#3 (Figure 5.6) was tested under high electric field conditions and lower electric field conditions to observe the sensor performance.

5.4.1 Sensor measurements over 1 kV/m

Figure 5.18 shows sensor output for a 0 - 120 kV/m case for two bias voltages (V_{m1} and V_{m2}). It can be seen that the sensor output is linear and the sensitivity is proportional to electrode bias.

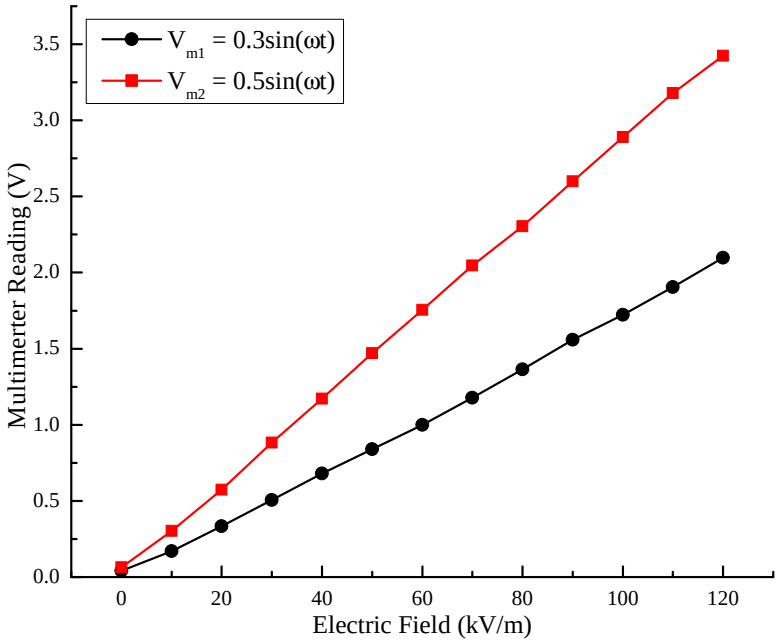

FIGURE 5.18: Sensor#3 response to higher electric fields.

5.4.2 Sensor measurements under 1 kV/m

Figure 5.19 shows sensor output with lower electric field conditions. It can be seen that sensor has a slight non-linearity at very low electric field condition. Non-zero result for zero incident dc field is due to a secondary dc electric field originating from the grounded sensor mount. When the measuring field is significant than secondary dc electric field, sensor output becomes linear. Table 5.2 lists the sensor responses under 1 kV/m electric fields.

TABLE 5.2: Sensor#3 response to electric fields under 1 kV/m

Electric field (V/m)	Multimeter reading (V)
0	0.456
10	0.461
50	0.480
100	0.500
500	0.656
1000	0.846

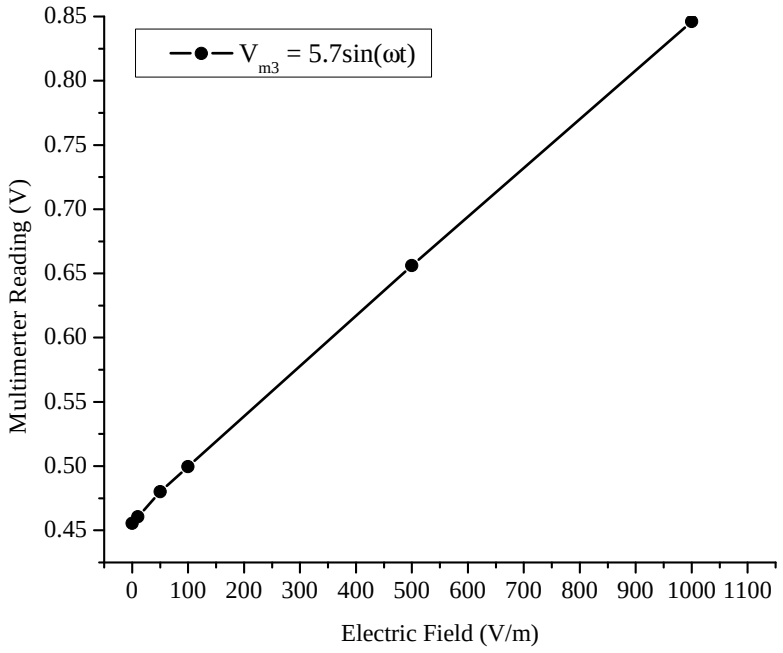

FIGURE 5.19: Sensor#3 response to lower electric fields.

5.4.3 Sensitivity calculation

5.4.3.1 Sensor sensitivity

Sensitivity is the smallest measurement that can be detected from a sensor or a instrument. From the Figure 5.19, slope can be considered as the sensitivity (S). Data in Table 5.2 shows that for a 100 V/m electric field, the sensor output is 500 mV, and for a 1000 V/m electric field, the sensor output is 846 mV. Therefore, the sensitivity of sensor#3 can be determined as,

$$S = \frac{846 - 500}{1000 - 100} = 0.38 \qquad [\text{mV/(V/m)}] \quad (5.1)$$

It should be noted that, the sensitivity can be changed by changing the bias voltage. Highest sensitivity that can be achieved with the developed electronics is 0.38 $mV/(V/m)$.

5.4.3.2 Sensor resolution

The resolution of a sensor is the smallest increment of change in the measurement that can be determined from the readout. When the sensor was biased at it maximum operating voltage (11.2 V_{pp}), noise envelope was measured to be 1.6 mV. When the electric field was changed from 10 V/m, considering the first two data points from Table 5.2, noise limited resolution (E_{min}) can be calculated as,

$$E_{min} = \frac{1.6\,\mathrm{mV}}{5\,\mathrm{mV}} \times 10\,\mathrm{V/m} = 3.2 \qquad [\mathrm{V/m}] \quad (5.2)$$

5.5 High voltage lab experiments

High voltage lab experiments were performed to identify sensor performance, robustness of the system and reliability of the measurements under actual field situations at University of Manitoba High Voltage Lab. Portable box to HVdc line distance was maintained at 53 cm. High voltage system has capability of producing 0 -25 kV variable voltages and test was performed changing the amplitude of the dc line voltage in discrete intervals. Figure 5.20 shows the lab set up. Portable box is placed inside a hole under the ground surface. Metal sheet is grounded to create a known uniform electric field.

5.5.1 Electric field distribution calculation under a power line

The electric field under a current carrying conductor can be calculated using the image method of charges. When the power line voltage is V_0 and λ is the charge

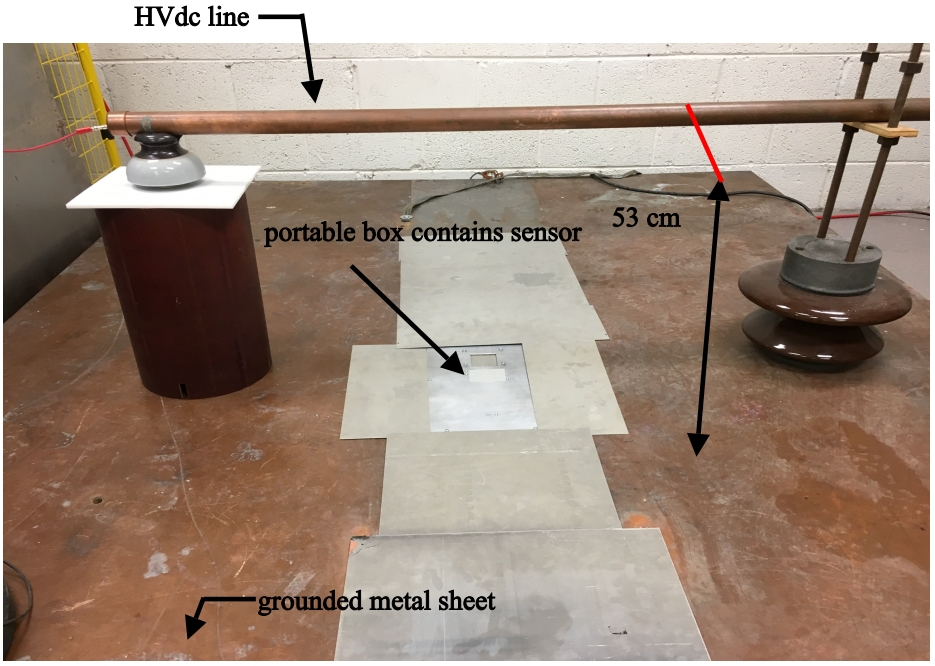

FIGURE 5.20: High voltage lab test setup.

per unit length, this situation can depicts as Figure 5.21.

The work done against the field per unit charge moving from A (*initial*) to B (*final*) is given by the line integral as shown in the Equation 5.3,

$$V_{final} - V_{inital} = -\int \vec{E}.\vec{ds} = -\int (E_{Q1} + E_{Q2}).ds \tag{5.3}$$

$$V_B - V_A = (\int_{Q1} \frac{\lambda}{2\pi\varepsilon_0 s_1}.ds - \int_{Q2} \frac{\lambda}{2\pi\varepsilon_0 s_2}.ds) \tag{5.4}$$

$$V_B - V_A = (\int_0^s \frac{\lambda}{2\pi\varepsilon_0 (d-s)}.ds - \int_0^s \frac{\lambda}{2\pi\varepsilon_0 (d+s)}.ds) \tag{5.5}$$

$$V_B|_s = \frac{\lambda}{2\pi\varepsilon_0}(\ln(d+s) - \ln(d-s)) \tag{5.6}$$

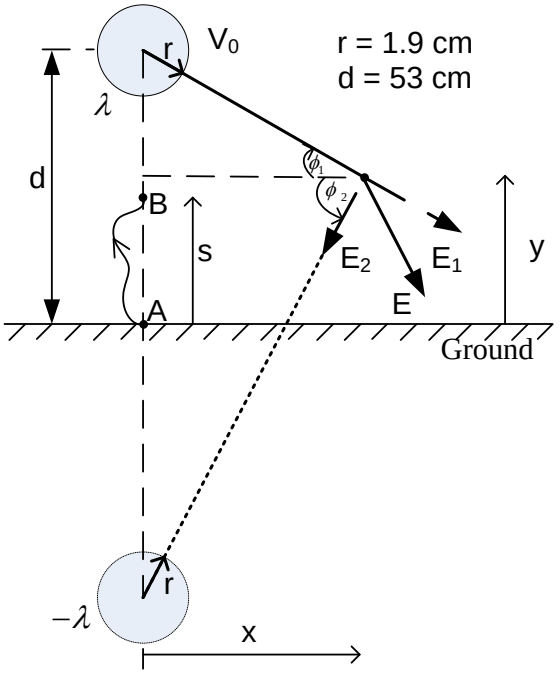

FIGURE 5.21: Electric field calculation: Image conductor method.

$$V_B|_s = \frac{\lambda}{2\pi\varepsilon_0} \ln(\frac{d+s}{d-s}) \tag{5.7}$$

when $s = d - r$, $V_B|_{(s=d-r)} = V_0$ and

$$V_0 = \frac{\lambda}{2\pi\varepsilon_0} \ln(\frac{2d-r}{r}) \quad [\text{V}] \tag{5.8}$$

Let's consider a point at (x, y) coordinate under a the power line as shown from the Figure 5.21.

$$\phi_1 = \arctan \frac{d-y}{x} \tag{5.9}$$

$$\phi_2 = \arctan \frac{d+y}{x} \tag{5.10}$$

$$\phi = \phi_1 + \phi_2 = \arctan\frac{d-y}{x} + arctan\frac{d+y}{x} \tag{5.11}$$

$$|E|^2 = |E_1|^2 + |E_2|^2 + 2|E_1||E_2|\cos(\phi) \tag{5.12}$$

$$|E_1| = \frac{\lambda}{2\pi\varepsilon_0} \times \frac{1}{\sqrt{x^2 + (d-y)^2}} \tag{5.13}$$

$$|E_2| = \frac{\lambda}{2\pi\varepsilon_0} \times \frac{1}{\sqrt{x^2 + (d+y)^2}} \tag{5.14}$$

$$|E|^2 = (\frac{\lambda}{2\pi\varepsilon_0})^2\{(\frac{1}{x^2+(d-y)^2}+\frac{1}{x^2+(d+y)^2})+2\frac{1}{\sqrt{x^2+(d-y)^2}}\cdot\frac{1}{\sqrt{x^2+(d+y)^2}}\cdot\cos(\phi)\} \tag{5.15}$$

equation 5.8 can be written as

$$\frac{\lambda}{2\pi\varepsilon_0} = \frac{V_0}{\ln(\frac{2d-r}{r})} \tag{5.16}$$

if $y = 0$ and $x = 0$,

$$|E| = \frac{V_0}{\ln(\frac{2d-r}{r})} \times \frac{2}{d} \tag{5.17}$$

For example, When the sensor is placed just below the power line and assume $V_0 = 1$ kV, electric field can be calculated substituting values to the Equation 5.17,

$$E_{1kV} = \frac{1000}{\ln(\frac{2\times0.53-0.019}{0.019})} \times \frac{2}{0.53} = 942.6 \text{ V/m}$$

5.5.2 Simulation of HV lab setup

Lab set up was simulated using COMSOL multiphysics software to validate calculations and determine electric field behaviour a under power line. Simulation was done inside a $10 \times 10 \times 10\ m^3$ air box with taking actual physical parameters of the HVdc line. Figure 5.22 shows the simulation set-up.

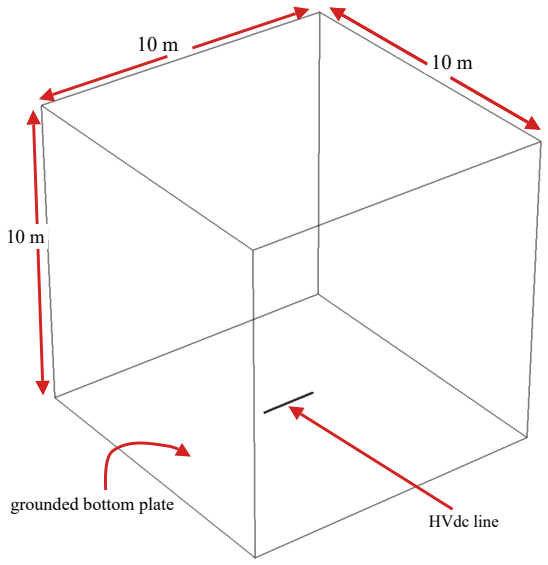

FIGURE 5.22: COMSOL simulation set-up for mock HVdc line.

Figure 5.23 shows a 2D graph of electric field distribution over the ground surface under the power line and Figure 5.24 shows the electric field distribution over the ground surface in a cross sectional view to the power line. It can be seen that the electric field is at its maximum under the power line. When the HVdc line is energized to 1 kV, simulations shows 942 V/m electric field just above the ground surface under the power line. Further, it can be noted that the electric field has a non-linear relationship with distance when moving away from the power line.

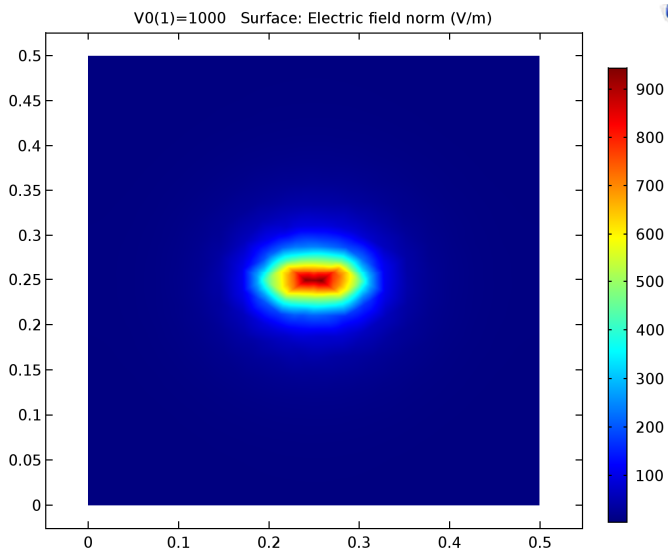

FIGURE 5.23: Electric field distribution over the ground surface.

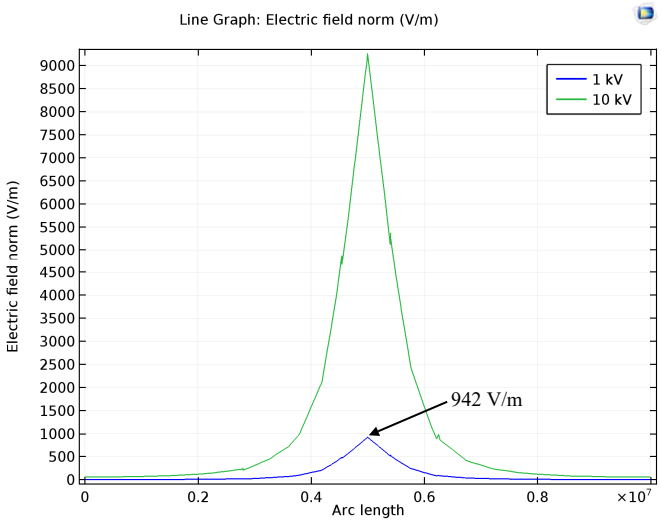

FIGURE 5.24: Electric field distribution over the ground surface when the power line at 1 kV and 10 kV cases.

According to the Equation 5.17 and simulation results, it can be concluded that calculated electric field is agreed with the simulation result.

5.5.3 Testing under a HVdc line

In this test, sensor#3 was examined under different electric field conditions of the HVdc line. The sensor was biased at $3.5\sin(2\pi 597t)$ and Figure 5.25 shows the sensor responses. According to the figure sensor is showing a linear relationship with the measured field.

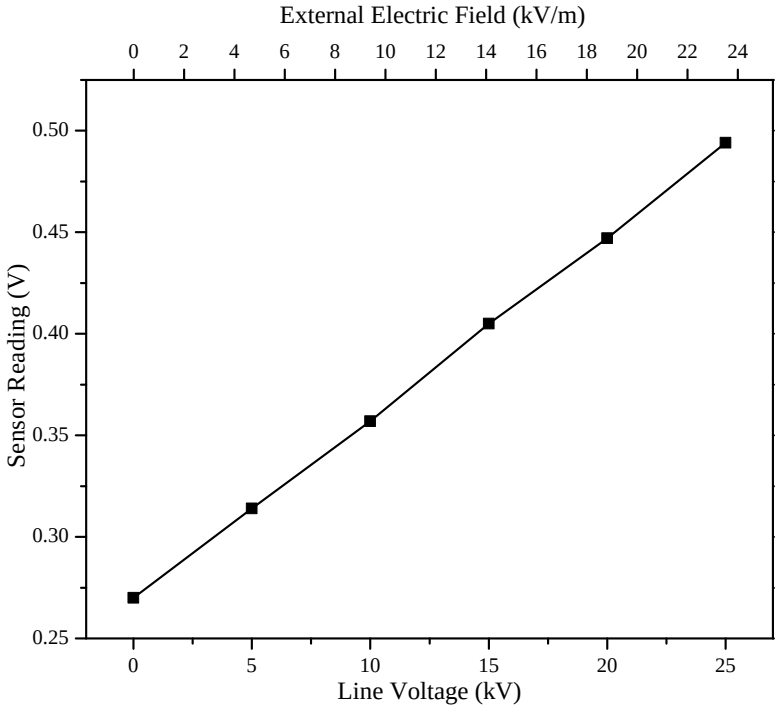

FIGURE 5.25: High voltage lab test with different dc electric fields.

Table 5.3 summarizes the calculated external electric field (outside the portable box) and the sensor responses. Actual electric field numbers were taken from the calculations and it can be slightly different with the lab environment. It can be seen from Table 5.3 when the HVdc line voltage at 0 V sensor is measuring a considerable electric field. This is due to sensor is measuring secondary electric fields by the sensor mount and possible iron charges in the lab environment.

TABLE 5.3: Electric field and sensor response comparison.

Line voltage (kV)	Calculated external electric field (V/m)	Sensor response (mV)
0	0	0.27
5	4713	0.314
10	9426	0.357
15	14139	0.405
20	18851	0.447
25	23564	0.494

5.5.4 Testing under the mock dc line with presence of space charges

In power industry, charge density per unit area under power lines is a important factor to ensure safety of operators and agriculture purposes. Due to intense electric field surrounding the high voltage lines, air become ionized and creates space charges [16, 29, 30] .

5.5.4.1 Procedure

In this experiment, metal rings with sharp edges were attached to the mock dc line to create space charges. When the dc line in high potential (> 10 kV), ionized ions (space charges) were expected to be around the test set-up creating an ironic rain. Figure 5.26 shows the experimental lab set-up.

First of all, sensor was calibrated with a 800 V/m electric field. Then, the window was opened for external field measurements. Then the power line was energized to 15 kV for $\sim$4 minutes and switched off for $\sim$1 minute. Finally, window was closed and data was saved using the developed electronics. Data was sampled at 2 s intervals.

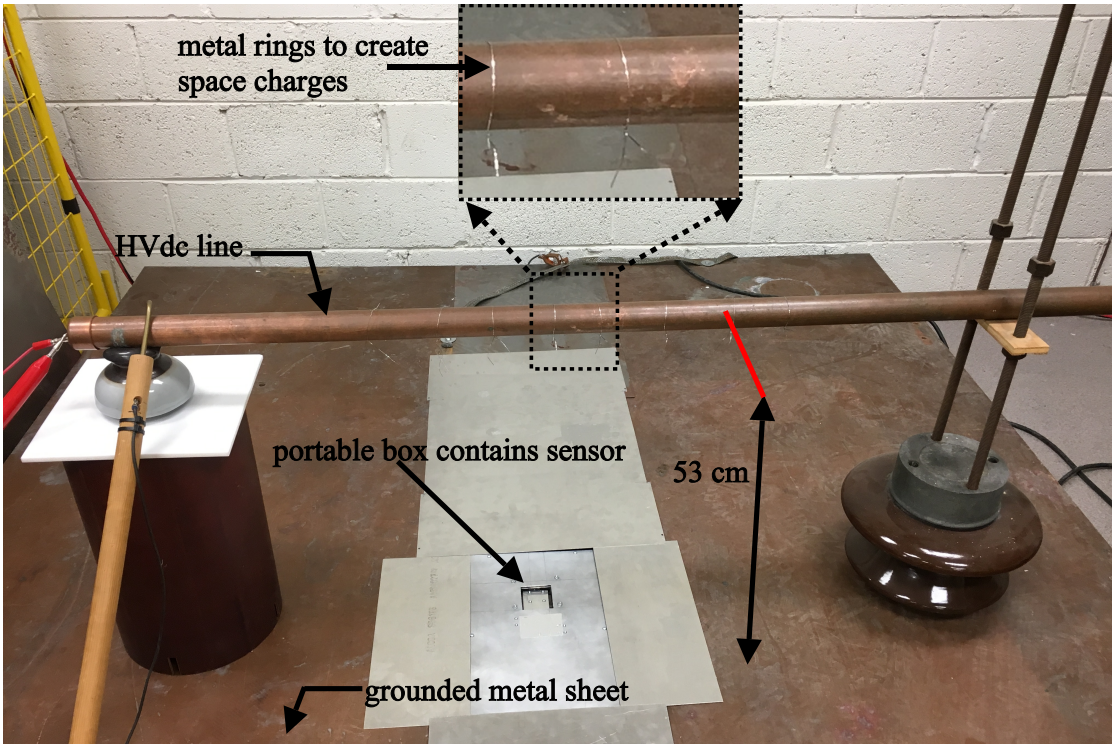

FIGURE 5.26: High voltage test set-up for space charge density measurement.

5.5.4.2 Results

Figure 5.27 compares the sensor response in the event of with and without corona presence. Red dashed line compares the sensor measurement without corona presence. It can be seen from Figure 5.27, after window was opened, sensor was measuring a electric field in the environment without applying a potential to the dc line. Furthermore, it should be noted that, the average sensor response without corona presence is 400 mV. However, when corona presence and power line is energized to the same voltage, sensor measures an extremely high electric field due to ionized charges. When the mock power line is brought to zero voltage, sensor response dropped by around 300 mV, that is a similar response for $\sim$ 800 V/m field. In this condition, sensor measures collected space charges on the floating *Al* metal plate. After the floating plate was grounded, sensor measures zero field

condition. This observation concludes that no residual charges or trapped charges stayed inside the box or on the sensor when the floating plate was grounded. Finally, charge collected over the floating *Al* plate can be calculated and it can be expressed as the charge density per unit area under the power line. Charge density calculation under a power line is suggested as a future work.

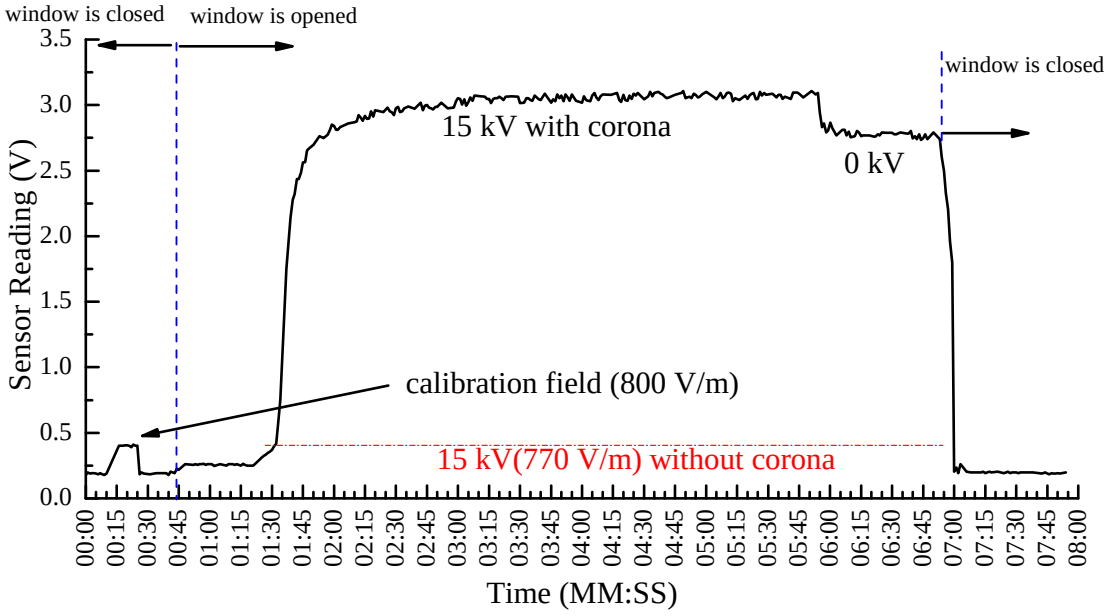

FIGURE 5.27: High voltage lab experiment when the corona presence with the developed portable system.

Chapter 6

Conclusion and Future Work

6.1 Conclusion

This thesis successfully demonstrated a novel dc electric field sensor using a torsional micro mirror and the met all the objectives were listed in Chapter 1.

Chapter 3 discussed about the sensor design and simulations. Due to differential bias technique, sensor does not need a ground reference for sensor operation. This is an advantage because it enables easy measurements and resolves the grounding related problems of current state of the art sensors. Furthermore, the sensor response can dynamically change according to the electric field situation.

In Chapter 4, sensor fabrication process was explained overcoming the fabrication challenges. Furthermore, to reduce the cost of fabrication, normal Si wafers were used instead of SOI wafers. Also, to reduce the complexity of fabricating the sensors the bulk micro-machining technique was used. A new, low stress fabrication process was developed to design the reflective mirrors.

Chapter 5 discussed about sensor measurements, successful design of the portable system for outdoor measurements, and the measurements under a mock power line. Developed torsional mirror sensors are capable of the measuring dc fields from 10's of V/m to MV/m range. The portable sensor box, which is powered by 6V batteries, is capable of visualizing and storing data, changing frequency and sensor bias voltage, and changing the sampling frequency of the sensor measurement. The sensor was tested under a mock dc line, with and without corona presence and it effectively identified changes in the environment due to space charges in a field with corona presence. The added calibration voltage plate in the measuring system can be used to calibrate the sensor before measuring the incident field making the measurement more reliable and accurate.

6.2 Future Work

This sensor system can be improved in several ways. To optimize the electric field sensor box design optimal distance from the sensor and the box opening should be calculated. Furthermore, more robust software and hardware must be developed for implementation in industrial applications. A further area for improvement is testing the sensors separately to reduce electric interference from nearby sensors. Furthermore, the sensor should be tested under an actual dc transmission line determine the accuracy and reliability of the sensor readings in a natural environment and improve its effectiveness. Also, this sensor should be tested in different industrial measurements and calibrated for specific situations.

6.3 Other Applications

In this study, the torsional mirror sensor was used and developed for the purpose of dc power line monitoring. However, this sensor can be applied in various other situations.

In atmospheric science, for example. electric field measurements are used to predict weather phenomena like lightning. Using measurements from different locations, meteorologists can predict which areas will be affected by lightning strikes. Furthermore, electric field measurements can help aerospace companies to avoid thunderstorms when launching rockets. Electric field measurements can also detect and control static charges. For example, when transporting electrostatically charged chemicals or flammable liquids such as fuel, it is important to measure the static charge level frequently in order to avoid hazardous conditions, [7, 31]. The current sensor does not require grounding and can be used for longer durations, so it can provide accurate measurements to improve safety conditions in these areas.

Also, electric field intensity measurements can be used to measure planetary emissions and to observe planetary electric field patterns during planetary exploration missions. In biological and medical science, electric field measurements are used to measure conditions of cells and to characterize particular cells. ECG (electrocardiography) tests utilizes electric field measurements to measure, cardiac cell's depolarization and the re-polarization during a normal cycle. The current sensor allows for precise and accurate measurements at lower costs, and which would facilitate various scientific endeavours and other industry applications.

Today, dc power has many applications. For instance it is being used in batteries in electric vehicles, solar powered homes etc. In the near future, houses

will have one central ac/dc power converter that will send dc power to all the devices in the house. Instead of installing a converter in each device, only one converter will be needed. Essentially, dc power is expected to be the future and compact voltage meters will be needed to measure and sense voltages levels.

The developed sensor provides increased accuracy and safety in dc field measurements and advance applications in other fields. The improved usage flexibility of the current sensor and its broad applicability at lower costs and more convenience make this sensor an alternative to exiting electric field sensors available in the market today.

Appendix A

Simulation

A.1 Two spring sensor performance comparison with vertical and torsional moving types

This section investigates how the two spring sensor perform better in torsional type than the vertical type in side the acrylic frame design. The vertical motion of the sensor was achieved by applying a same bias voltage to two electrodes on the sensor.

The sensor#3 was simulated under a same electric field condition for both cases and mirror deformation was measured. Figure A.1 shows the simulation results for the sensor was biased with differential 1 V. This leads to sensor to operate in the torsional motion. In this figure, sensor deformation is scaled by 500000 to clearly see the sensor deformation. Figure A.1 shows sensor vertical motion. As well, in this figure, since the sensor motion is small, therefore, the sensor deformation is scaled by 500000.

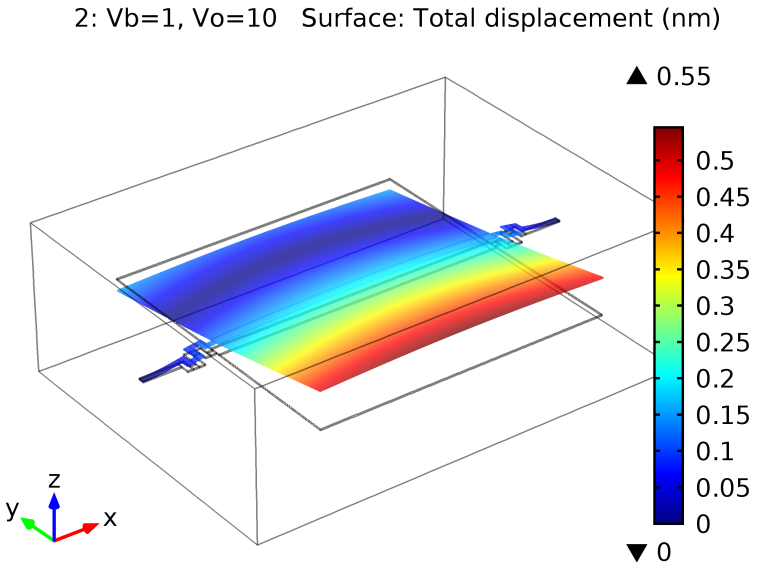

FIGURE A.1: Two spring sensor torsional motion

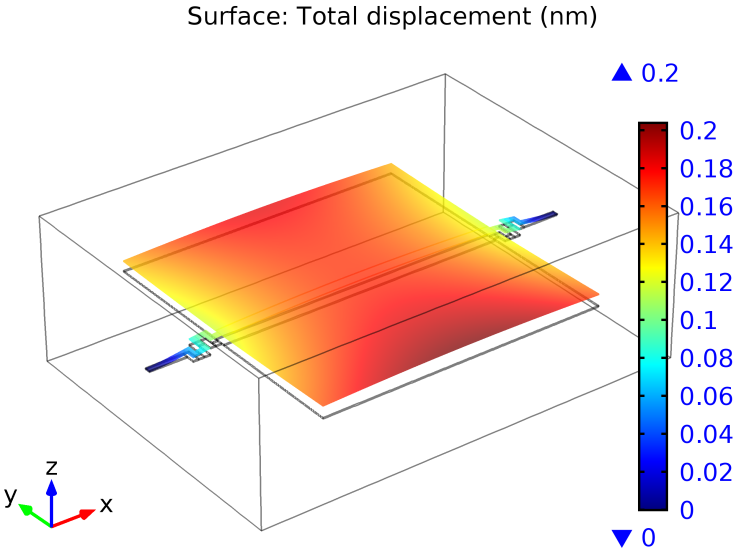

FIGURE A.2: Two spring sensor vertically up motion

Acrylic frame is designed to bounce laser beam on the sensor and detect the reflected laser from a photo diode. With compared to the sensor developed by Chen at el. [7], torsional sensor gives superior results using the same acrylic design for a lower sensor bias. This is due to torsional motion causes to move laser beam a longer distance on the photo-diode than the vertical moving sensor type.

Figure A.3 shows laser beam motion according to the simulations results. It can be seen that torsional type has 3 times better sensitivity than the vertical sensor type for the distance shown in the figure. Increasing the distance from sensor to the photo-detector, torsional sensor sensitivity can be improved.

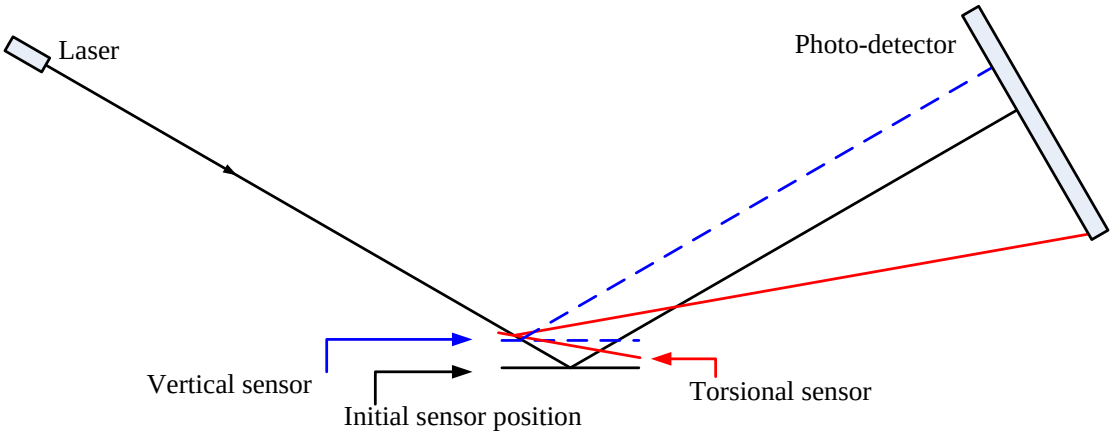

FIGURE A.3: Torsional sensor response with compared to vertical sensor.

Appendix B

Fabrication

B.1 Stress in thin films

Figure B.1 demonstrates material behaviour under tensile and compressive stress behaviour.

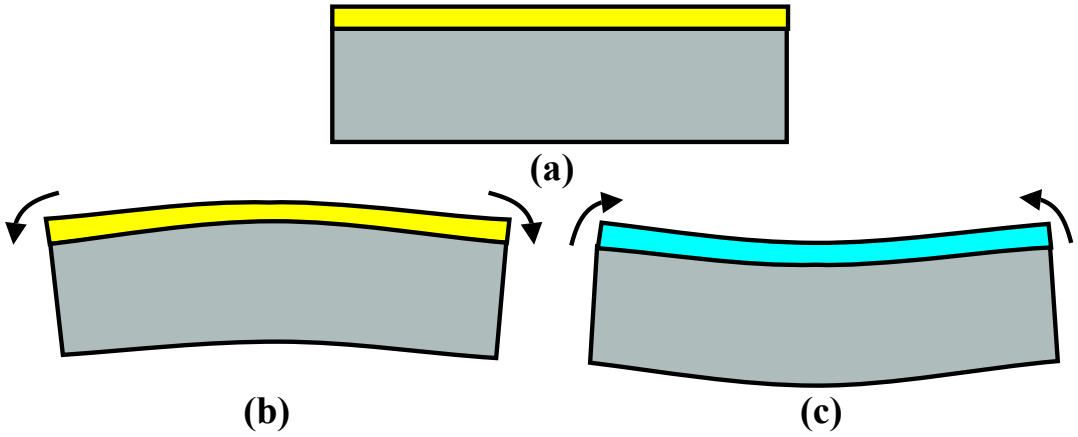

FIGURE B.1: Stress in thin films (a) Material deposition at elevated temperature (b) residual compressive stress at room temperature trying to expand (c) residual tensile stress at room temperature trying to shrink

B.2 Oxidation tray arrangement

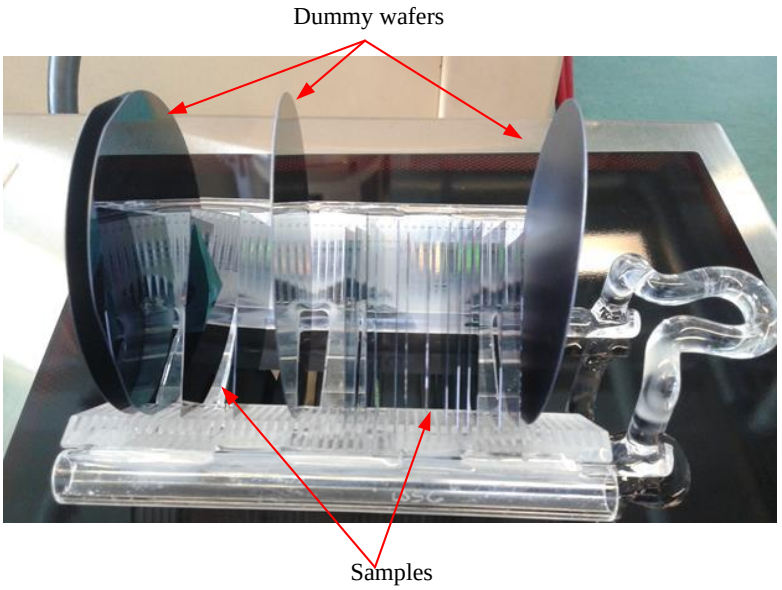

FIGURE B.2: Best technique for sample arrangement in wet oxidation tray.

B.3 Measurement techniques with Instruments

To verify the dimensions of the sensors (or devices) the relevant parameters were measured at each step of the fabrication process and after the fabrication process was completed.

Alpha step 500 instrument (Figure B.3 (a)) was used to the measure etched or deposited thickness of materials. M-2000D Ellipsometer (Figure B.3 (b)) was used to measure the thickness of the transparent materials such as SiO_2 and photoresit.

Wrong measurements can result in destroying or breaking the samples in the next step. Correct measurement techniques avoid wrong measurement results.

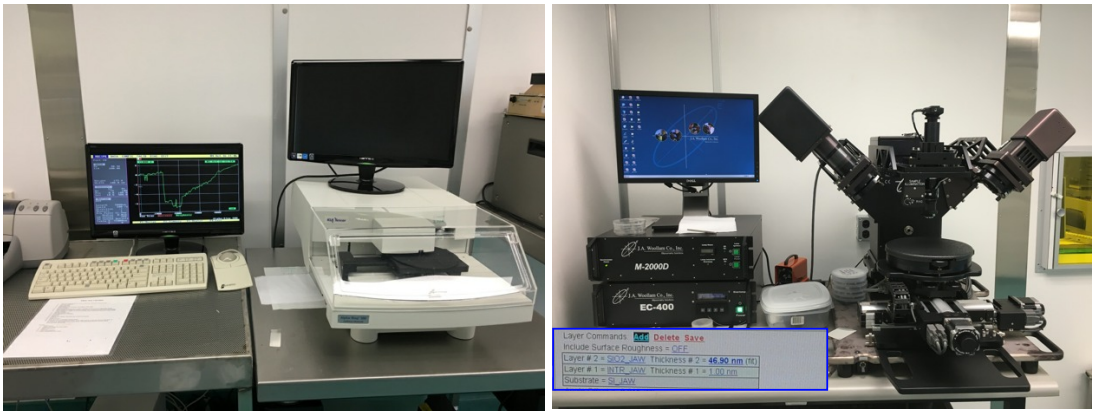

(a) (b)

FIGURE B.3: Measurement instruments :(a) Tencor Alpha Step 500 surface profiler (b) M-2000D Ellipsometer, sample result for SiO_2 is shown inside the blue box

Figure B.4 shows an example of sample thickness measurement using Alpha Step 500 surface profiler.

1. Sample should be laid on a cleaned dummy Si wafer. (This case 3" wafer is used.)

2. Sample should be tightly attached to the holding wafer using blue tape used in clean room.

3. Measurement should be taken very close to the blue tape as shown in the figure. Measurements taken away from the tape will prone to errors giving higher thickness.

4. Average of three (3) measurements taken at same place should be considered as the correct measurement.

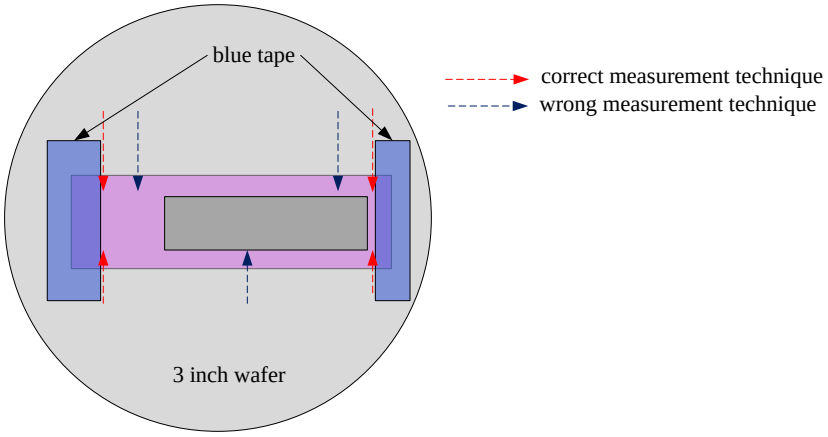

FIGURE B.4: Alpha step correct measurement technique

B.4 Epoxy Bonding

Aluminium can not solder with Lead (Pb) to wires. Therefore, conductive epoxy bonding method is used to glue wires to the aluminium pads. EPO-TEC H20E product was used with mixing its two components together in 1:1 ratio. Then, bond was cured in a oven at 80 °C for three(3) hours. Figure B.5 shows a thermally cured sample with epoxy bonding.

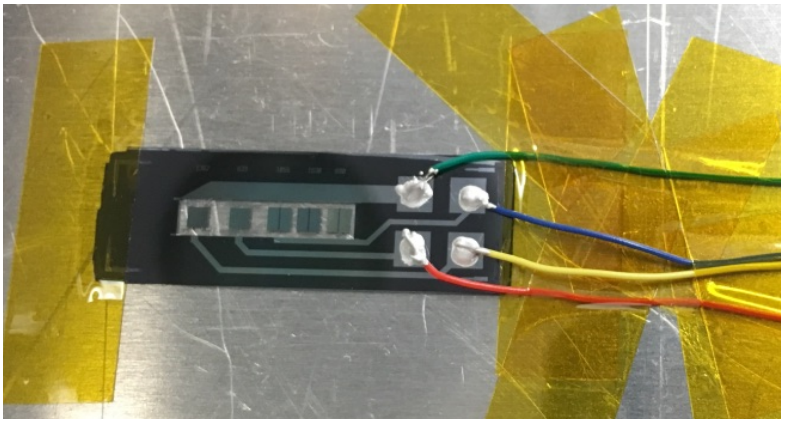

FIGURE B.5: Epoxy bonded sample with metal wires.

Appendix C

Electronic drawings

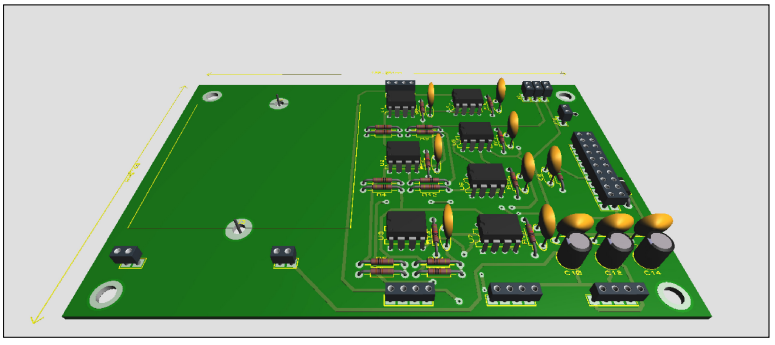

FIGURE C.1: Current to voltage converter 3D realisation

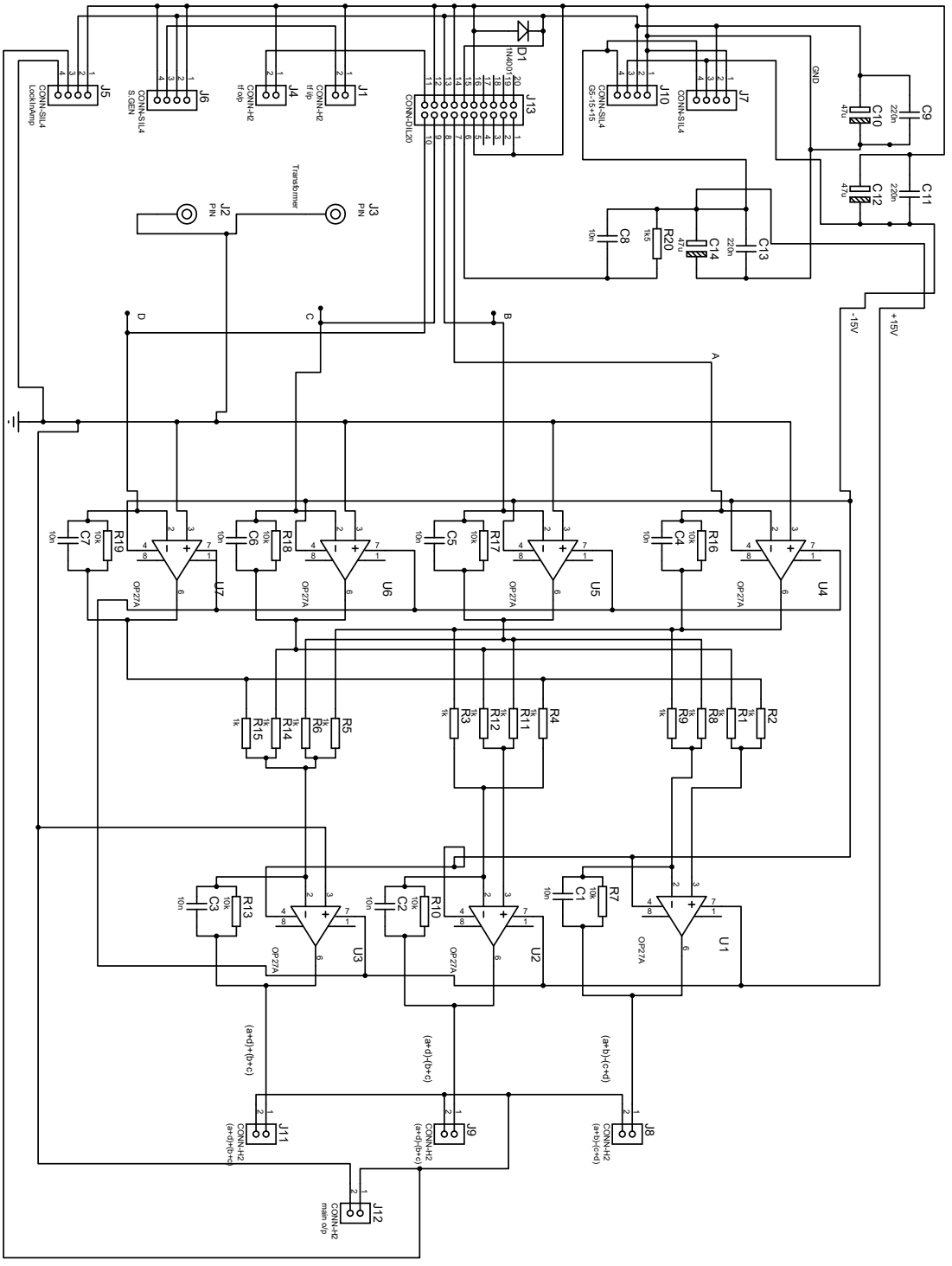

FIGURE C.2: Current to voltage converter Schematic for four split photo detector

References

[1] Yu Zhou. *Investigation of a Micromachined Electric Field Mill to Maximize the Electrostatic Field Sensitivity*. Department of Electrical and Computer Engineering, University of Manitoba, Winnipeg, Manitoba, 2011. URL `http://mspace.lib.umanitoba.ca/handle/1993/8922`.

[2] B. Bahreyni, G. Wijeweera, C. Shafai, and A. Rajapakse. Analysis and design of a micromachined electric-field sensor. *Journal of Microelectromechanical Systems*, 17(1):31–36, Feb 2008. ISSN 1057-7157. doi: 10.1109/JMEMS.2007.911870.

[3] Mark N. Horenstein and Patrick R. Stone. A micro-aperture electrostatic field mill based on {MEMS} technology. *Journal of Electrostatics*, 51–52:515 – 521, 2001. ISSN 0304-3886. doi: http://dx.doi.org/10.1016/S0304-3886(01)00048-1. URL `http://www.sciencedirect.com/science/article/pii/S0304388601000481`. Electrostatics 2001: 9th International Conference on Electrostatics.

[4] S. Ghionea, G. Smith, J. Pulskamp, S. Bedair, C. Meyer, and D. Hull. Mems electric-field sensor with lead zirconate titanate (pzt)-actuated electrodes. In *2013 IEEE SENSORS*, pages 1–4, Nov 2013. doi: 10.1109/ICSENS.2013.6688131.

[5] Tao Chen. Mem electric field sensor using force deflection with capacitance interrogation. In *2013 IEEE Power Energy Society General Meeting*, pages 1–4, July 2013. doi: 10.1109/PESMG.2013.6672919.

[6] A. Roncin, C. Shafai, and D.R. Swatek. Electric field sensor using electrostatic force deflection of a micro-spring supported membrane. *Sensors and Actuators A: Physical*, 123–124:179 – 184, 2005. ISSN 0924-4247. doi: http://dx.doi.org/10.1016/j.sna.2005.02.018. URL `http://www.sciencedirect.com/science/article/pii/S0924424705000841`. Eurosensors {XVIII} 2004The 18th European conference on Solid-State Transducers.

[7] T. Chen, C. Shafai, A. Rajapakse, J.S.H. Liyanage, and T.D. Neusitzer. Micromachined ac/dc electric field sensor with modulated sensitivity. *Sensors and Actuators A: Physical*, 245:76 – 84, 2016. ISSN 0924-4247. doi: http://dx.doi.org/10.1016/j.sna.2016.04.054. URL `http://www.sciencedirect.com/science/article/pii/S0924424716301996`.

[8] Sampath Liyanage, Cyrus Shafai, Tao Chen, and Athula Rajapakse. Torsional moving electric field sensor with modulated sensitivity and without reference ground. *Proceedings*, 1(4), 2017.

[9] Gayan Wijeweera. *Design of A Micromachined Electric Field Sensor Using A Thermal Actuating Shutter*. Department of Electrical and Computer Engineering, University of Manitoba, Winnipeg, Manitoba, 2008. URL `http://mspace.lib.umanitoba.ca/handle/1993/21304`.

[10] N O Renno, J F Kok, H Kirkham, and S Rogacki. A miniature sensor for electrical field measurements in dusty planetary atmospheres. *Journal of Physics: Conference Series*, 142(1):012075, 2008. URL `http://stacks.iop.org/1742-6596/142/i=1/a=012075`.

[11] Ehsan Tahmasebian. *Design, Modeling and Fabrication of a Copper Electroplated MEMS, Membrane Based Electric Field Sensor*. Department of Electrical and Computer Engineering, University of Manitoba, Winnipeg, Manitoba, 2014. URL `http://mspace.lib.umanitoba.ca/handle/1993/30182`.

[12] Andrew Roncin. *Design of a Microelectromechanical Transducer for electric Field measurement*. Department of Electrical and Computer Engineering, University of Manitoba, Winnipeg, Manitoba, 2004. URL `https://mspace.lib.umanitoba.ca/handle/1993/15777`.

[13] R. Miles, T. Bond, and G. Meyer. Report on non-contact dc electric field sensors. June 2009. URL `https://e-reports-ext.llnl.gov/pdf/374701.pdf`. LLNL-TR-414129.

[14] Z. Gao, Z. Yu, R. Zeng, F. Tian, J. Yu, M. Dai, B. Niu, M. Li, L. Liu, R. Li, and Y. Liao. Research on measuring methods and sensors of high voltage dc electric field. In *2014 International Conference on Information Science, Electronics and Electrical Engineering*, volume 2, pages 850–854, April 2014. doi: 10.1109/InfoSEEE.2014.6947787.

[15] K. Hidaka. Progress in japan of space charge field measurement in gaseous dielectrics using a pockels sensor. *Electrical Insulation Magazine, IEEE*, 12 (1):17–28, January 1996. ISSN 0883-7554.

[16] G. Zorpette. Hvdc: Wheeling lots of power. *IEEE Spectrum*, 22(6):30–36, June 1985. ISSN 0018-9235. doi: 10.1109/MSPEC.1985.6370491.

[17] S. P. Hornfeldt. Dc-probes for electric field distribution measurements. *IEEE Transactions on Power Delivery*, 6(2):524–529, Apr 1991. ISSN 0885-8977. doi: 10.1109/61.131106.

[18] I. Zaldivar-Huerta and J. Rodriguez-Asomoza. Electro-optic e-field sensor using an optical modulator. In *14th International Conference on Electronics, Communications and Computers, 2004. CONIELECOMP 2004.*, pages 220–222, Feb 2004. doi: 10.1109/ICECC.2004.1269576.

[19] K. Johansson, L. Walfridsson, U. Gafvert, B. Kallstrand, and S. Hornfeldt. Probe for measurements of the dc electric field in air around high voltage apparatus. pages 1–4. IEEE Publishing, October 2010. ISBN 978-1-4244-9468-2.

[20] Pengfei Yang, Chunrong Peng, Haiyan Zhang, Shiguo Liu, Dongming Fang, and Shanhong Xia. A high sensitivity soi electric-field sensor with novel comb-shaped microelectrodes. pages 1034–1037. IEEE Publishing, June 2011. ISBN 978-1-4577-0157-3.

[21] T. Kobayashi, S. Oyama, N. Makimoto, H. Okada, T. Itoh, and R. Maeda. An electrostatic field sensor operated by self-excited vibration of mems-based self-sensitive piezoelectric microcantilevers. *Sensors & Actuators: A. Physical*, 198:87–90, August 2013. ISSN 0924-4247.

[22] D Flandre. *Micromachined Thin-Film Sensors for SOI-CMOS Co-Integration*. 2006. ISBN 0-387-28842-2.

[23] L. B Freund. *Thin Film Materials Stress, Defect Formation and Surface Evolution*. 2004. ISBN 0-521-52977-8.

[24] S. I. Jun, T. E. McKnight, A. V. Melechko, M. L. Simpson, and P. D. Rack. Characterisation of reactively sputtered silicon oxide for thin-film transistor fabrication. *Electronics Letters*, 41(14):822–823, July 2005. ISSN 0013-5194. doi: 10.1049/el:20051045.

[25] Analog Devices. Op27gpz. http://www.analog.com/media/en/technical-documentation/data-sheets/OP27.pdf, 2015. Rev. H.

[26] Microchip Technology Inc. Mcp3004/3008. http://ww1.microchip.com/downloads/en/DeviceDoc/21295d.pdf, 2008.

[27] Analog Devices. Ad9833. http://www.analog.com/media/en/technical-documentation/data-sheets/AD9833.pdf, 2012. Rev. E.

[28] Microchip Technology Inc. 7/8-bit single/dual spi digital pot with non-volatile memory, mcp414x/416x/424x/426x. http://ww1.microchip.com/downloads/en/DeviceDoc/22059b.pdf, 2008.

[29] A.P Fews, R.J Wilding, P.A Keitch, N.K Holden, and D.L Henshaw. Modification of atmospheric {DC} fields by space charge from high-voltage power lines. *Atmospheric Research*, 63(3–4):271 – 289, 2002. ISSN 0169-8095. doi: http://dx.doi.org/10.1016/S0169-8095(02)00041-8. URL http://www.sciencedirect.com/science/article/pii/S0169809502000418.

[30] S.S. Razavipour, M. Jahangiri, and H. Sadeghipoor. Electrical field around the overhead transmission lines. *International Journal of Mathematical, Computational, Physical, Electrical and Computer Engineering*, 6(2):168 – 171, 2012. ISSN PISSN:2010-376X, EISSN:2010-3778. URL http://waset.org/Publications?p=62.

[31] C. J. Dahn, B. N. Reyes, A. Kashani, and J. Finkelshtein. Electrostatic hazards of explosive, propellant and pyrotechnic powders. In *Electrical Overstress/ Electrostatic Discharge Symposium Proceedings. 1998 (Cat. No.98TH8347)*, pages 139–150, Oct 1998. doi: 10.1109/EOSESD.1998.737033.